

Università degli studi di Padova
Dipartimento di Fisica e Astronomia

Tesi di Dottorato

Search for heavy resonances decaying into a Z boson and a vector boson in the $\nu\bar{\nu}$ $q\bar{q}$ final state at CMS

Supervisor: Prof. Franco Simonetto
Candidate: Lisa Benato

Scuola di Dottorato di Ricerca, XXX ciclo

"I have no special talent. I am only passionately curious."
(A. Einstein)

Contents

1	Introduction	1
2	Theoretical motivation	3
2.1	Beyond Standard Model theories	3
2.2	Heavy Vector Triplet	5
2.2.1	Simplified Lagrangian	5
2.2.2	Mass eigenstates, mixing parameters and decay widths	6
2.2.3	HVT production	10
2.2.4	Benchmark model A: weak coupling scenario	11
2.2.5	Benchmark model B: strong coupling scenario	12
2.2.6	Search for HVT resonances at LHC	13
2.3	Warped extra dimension	16
2.3.1	Randall-Sundrum original model (RS1)	16
2.3.2	Bulk extension of RS1: graviton production and decays	19
2.3.3	Search for KK bulk gravitons at LHC	22
3	The Large Hadron Collider and the CMS experiment	25
3.1	The Large Hadron Collider	25
3.1.1	Proton-proton interactions	28
3.2	CMS detector	29
3.2.1	The coordinate system	30
3.2.2	The magnet	31
3.2.3	The tracking system	31
3.2.4	The electromagnetic calorimeter	34
3.2.5	The hadronic calorimeter	35
3.2.6	The muon system	36
3.2.7	The trigger system and data acquisition	37
3.2.8	Particle Flow event reconstruction	38
3.2.9	Physics objects	39
3.3	ATLAS, ALICE, LHCb detectors	46
3.3.1	ATLAS	46

3.3.2	ALICE	47
3.3.3	LHCb	47
4	Search for diboson resonances in the $ZV \rightarrow \nu\bar{\nu}q\bar{q}$ final state	49
4.1	Data and Monte Carlo samples	50
4.2	Event selection	51
4.2.1	Vertex and Pile-up	51
4.2.2	Electrons	51
4.2.3	Muons	52
4.2.4	Taus	54
4.2.5	Photons	54
4.2.6	Jets	55
4.2.7	Jet mass	57
4.2.8	Jet substructure	58
4.2.9	b-tagging	59
4.2.10	Missing Energy	59
4.3	Diboson candidate reconstruction	61
4.4	Background estimation	62
4.5	Systematic uncertainties	63
4.6	Results	64
5	Combination of diboson searches in semileptonic final states	65
6	Conclusions	67

CONTENTS

1

Abstract

2

3

CONTENTS

Introduction

7 This analysis searches for signal of heavy resonances decaying into a pair of heavy vector
8 bosons. One Z boson is identified through its invisible decay ($\nu\nu$), while the other is required
9 to decay hadronically into a pair of quarks. The final states probed by this analysis therefore
10 consists in two quarks and two neutrinos, reconstructed as missing transverse energy (met).
11 The hadronically decaying boson (Z, W) is reconstructed as a fat jet, whose mass is used to
12 define the signal region. Two purity categories are exploited, based on the n-subjettiness of the
13 fat jet.

14 The search is performed by examining the distribution of the diboson reconstructed trans-
15 verse mass of the resonance VZ (mtVZ) for a localized excess. The shape and normalization
16 of the main background of the analysis (V+jets) are estimated with an hybrid approach using
17 the distribution of data in the sidebands, corrected for a function accounting for potential
18 differences between the signal region and the sidebands, while the minor background sources
19 are taken from simulations.

Theoretical motivation

23 The standard model (SM) of particles represents, so far, the best available description of the
 24 particles and their interactions. It is the summation of two gauge theories: the electroweak
 25 interaction, that portrays the weak and electromagnetic interactions together, and the strong
 26 interaction, or Quantum Chromodynamics (QCD). Particles, namely quarks and leptons, are
 27 described as spin 1/2 fermions, whilst interactions are represented by spin 1 bosons. The
 28 symmetry group of the standard model is:

$$SU_C(3) \times SU_L(2) \times U_Y(1), \quad (2.1)$$

29 where the first factor is related to strong interactions, whose mediators are eight gluons,
 30 while $SU_L(2) \times U_Y(1)$ is the electroweak symmetry group, whose mediators are photons and
 31 Z - W^\pm bosons.

32 In renormalizable theories, with no anomalies, all gauge bosons are expected to be massless,
 33 in contrast with our experimental knowledge. This inconsistency is solved by introducing a
 34 new scalar particle, the Higgs boson, that can give mass to weak bosons and fermions via the
 35 spontaneous symmetry breaking mechanism.

36 In the last decades, Standard Model has been accurately probed by many experimental
 37 facilities (LEP, Tevatron, LHC), and the results lead to an impressive agreement between
 38 theoretical predictions and experiments. The discovery of the Higgs boson at the CERN Large
 39 Hadron Collider, measured by both CMS and ATLAS collaborations [1–7], represents not only
 40 an extraordinary confirmation of the model, but also the latest biggest achievement in particle
 41 physics as a whole.

43 2.1 Beyond Standard Model theories

44 Even though the Standard Model is the most complete picture of the universe of the particles,
 45 many questions are still left open. From a phenomenological point of view, some experimental
 46 observations are not included in the theory:

- 47 • in SM, neutrinos are massless (whilst experimentally their masses are confirmed to be
 48 non-zero, i.e. by the neutrino oscillations);

- 49 • no candidates for dark matter are predicted;
- 50 • no one of the fields included in the SM can explain the cosmological inflation;
- 51 • SM can not justify the matter-antimatter asymmetry.
- 52 From a purely theoretical perspective, some issues are still relevant in the formulation of the
53 model:
- 54 • *Flavour problem.*
55 The Standard Model has 18 free parameters: 9 fermionic masses; 3 angular parameters in
56 Cabibbo-Kobayashi-Maskawa matrix, plus 1 phase parameter; electromagnetic coupling
57 α ; strong coupling α_{strong} ; weak coupling α_{weak} ; Z mass; the mass of the Higgs boson.
58 Such a huge number of degrees of freedom marks the SM as weakly predictive in the
59 flavour sector.
- 60 • *Unification.*
61 There is not a “complete” unification of strong, weak and electromagnetic interactions,
62 since each one has its own coupling constant, behaving differently at different energy
63 scales; not to mention the fact that gravitational interaction is completely excluded from
64 the SM.
- 65 • *Hierarchy problem.*
66 From Quantum Field Theory, it is known that perturbative corrections to the mass of
67 the scalar bosons included in the theory tend to make it increase towards the energy
68 scale at which the considered theory still holds [8]. If the Standard Model is seen as
69 a low-mass approximation of a more general theory valid up to the Planck mass scale
70 (*i.e.*, $\sim 1.2 \times 10^{19}$ GeV), a fine-tuning cancellation of the order of 1 over 10^{34} is needed
71 in order to protect the Higgs mass at the electroweak scale (~ 100 GeV). Such an aston-
72 ishing correction is perceived as very unnatural.
- 73 Numerous Beyond Standard Model theories (BSM) have been proposed in order to over-
74 come the limits of the Standard Model.
- 75 Grand Unified Theories (GUT) aim at extending the symmetry group of the SM (eq. 2) into
76 largest candidates, such as $S0(10)$, $SU(5)$ and $E(6)$. At GUT scale, approximately at 10^{16} GeV,
77 non-gravitational interactions are expected to be ruled by only one coupling constant, α_{GUT} .
- 78 Super Symmetryc (SUSY) models state that every fermion (boson) of the Standard Model has a
79 bosonic (fermionic) superpartner, with exactly the same quantum numbers, except the spin. If
80 SUSY is not broken, each couple of partners and superpartners should have the same masses,
81 hypothesis excluded by the non-observation of the s-electron. Super Symmetry represents a
82 very elegant solution of the hierarchy problem of the Higgs boson mass, since the perturba-
83 tive corrections brought by new SUSY particles exactly cancel out the divergences caused by
84 SM particles corrections. A particular sub-class of SUSY models, Minimal Super Symmetric
85 Standard Models, is characterized by the introduction of a new symmetry, the R-parity, that
86 guarantees the proton stability and also the stability of the lightest SUSY particle, a possible
87 good candidate for dark matter.
- 88
- 89 Two other possible theoretical pictures are extensively described in sec. 2.2-2.3.

90 2.2 Heavy Vector Triplet

91 The heavy vector triplet model [9] provides a general framework aimed at studying new
 92 physics beyond the standard model, that can manifest into the appearance of new resonances.
 93 The adopted approach is that of the simplified model, in which an effective Lagrangian is
 94 introduced, in order to describe the properties and interactions of new particles (in this case,
 95 a triplet of spin-1 bosons) by using a limited set of parameters, that can be easily linked
 96 to the physical observables at the LHC experiments. These parameters can describe many
 97 physical motivated theories (such as sequential extensions of the SM [10, 11] or Composite
 98 Higgs [12, 13]).

99 Since a simplified model is not a complete theory, its validity is restricted to the on-shell
 100 quantities related to the production and decay mechanisms of the new resonances, that is how
 101 most of the LHC BSM searches are performed. Given these conditions, experimental results
 102 in the resonant region are sensitive to a limited number of the phenomenological Lagrangian
 103 parameters (or to a combination of those), whilst the remaining parameters tend to influence
 104 the tail of the distributions.

105 Limits on production cross-section times branching ratio ($\sigma\mathcal{B}$), as a function of the invariant
 106 mass spectrum of the probed resonance, can be extracted from experimental data. Given that
 107 $\sigma\mathcal{B}$ are functions of the simplified model parameters and of the parton luminosities, it is then
 108 possible to interpret the observed limits in the parameter space.

109 2.2.1 Simplified Lagrangian

110 The heavy vector triplet framework assumes the existence of an additional vector triplet, V_μ^a ,
 111 $a = 1, 2, 3$, in which two spin-1 particles are charged and one is neutral:

$$V_\mu^\pm = \frac{V_\mu^1 \mp i V_\mu^2}{\sqrt{2}}; \quad (2.2)$$

$$V_\mu^0 = V_\mu^3.$$

112
 113 The triplet interactions are described by a simplified Lagrangian, that is invariant under SM
 114 gauge and CP symmetry, and accidentally invariant under the custodial symmetry $SU(2)_L \times$
 115 $SU(2)_R$:

$$\begin{aligned} \mathcal{L}_V = & -\frac{1}{4} \left(D_\mu V_\nu^a - D_\nu V_\mu^a \right) \left(D^\mu V^\nu{}^a - D^\nu V^\mu{}^a \right) + \frac{m_V^2}{2} V_\mu^a V^\mu{}^a \\ & + ig_V c_H V_\mu^a \left(H^\dagger \tau^a D^\mu H - D^\mu H^\dagger \tau^a H \right) + \frac{g^2}{g_V} c_F V_\mu^a \sum_f \bar{f}_L \gamma^\mu \tau^a f_L \\ & + \frac{g_V}{2} c_{VVV} \epsilon_{abc} V_\mu^a V_\nu^b (D^\mu V^\nu{}^c - D^\nu V^\mu{}^c) + g_V^2 c_{VVH} V_\mu^a V^\mu{}^a H^\dagger H - \frac{g}{2} c_{VW} \epsilon_{abc} W^{\mu\nu}{}^a V_\mu^b V_\nu^c. \end{aligned} \quad (2.3)$$

116
 117 In the first line of the formula 2.3, V mass and kinematic terms are included, described with
 118 the covariant derivative $D_\mu V_\nu^a = \partial_\mu V_\nu^a + g \epsilon^{abc} W_\mu^b V_\nu^c$, where W_μ^a are the fields of the weak inter-
 119 action and g is the weak gauge coupling. V_μ^a are not mass eigenstates, since they mix with the
 120 electroweak fields after the spontaneous symmetry breaking, therefore m_V isn't the physical

121 mass of the V bosons.
 122 The second line describes the interaction of the triplet with the Higgs field and the SM left-
 123 handed fermions; c_H describes the vertices with the physical Higgs and the three unphysical
 124 Goldstone bosons that, for the Goldstone equivalence theorem, are equivalent to the longitu-
 125 dinal polarization of W and Z bosons at high-energy; hence, c_H is related to the bosonic decays
 126 of the resonances. c_F is the analogous parameter describing the V interaction with fermions,
 127 that can be generalized as a flavour dependent coefficient, once defined $J_F^{\mu a} = \sum_f \bar{f}_L \gamma^\mu \tau^a f_L$:
 128 $c_F V_\mu^a J_F^{\mu a} = c_\ell V_\mu^a J_\ell^{\mu a} + c_q V_\mu^a J_q^{\mu a} + c_3 V_\mu^a J_3^{\mu a}$.
 129 The last part of the equation includes terms that are relevant only in strongly coupled scenar-
 130 ios (see sec. 2.2.2.2) through the V - W mixing, but it does not include vertices of V with light
 131 SM fields, hence it can be neglected while describing the majority of the LHC phenomenol-
 132 ogy, under the assumptions previously stated. Additional dimension four quadrilinear V
 133 interactions are non relevant for the processes discussed, otherwise their effects would be ap-
 134 preciated in electroweak precision tests and precise Higgs coupling measurements [14].
 135

136 The parameters in the Lagrangian can be interpreted as follows: g_V describes the strength
 137 of the interaction, that is weighted by c parameters. g_V ranges from $g_V \sim 1$ when the coupling
 138 is weak (sec. 2.2.4), to $g_V \sim 4\pi$ when the coupling is strong (sec. 2.2.5). c parameters are
 139 expected to be $c \sim 1$, except to c_H , that can be smaller for weak couplings. The combinations
 140 describing the vertices, $g_V c_H$ and $g^2/g_V c_F$, can be considered as the fundamental parameters,
 141 used to interpret the experimental results.

142 2.2.2 Mass eigenstates, mixing parameters and decay widths

143 The newly introduced $SU(2)_L$ triplet is expected to mix with the weak SM fields. The $U(1)_{em}$
 144 symmetry is left unbroken by the new interaction, hence the massless combination of the
 145 electroweak fields, namely the photon, is the same as the SM:

$$A_\mu = B_\mu \cos \theta_W + W_\mu^3 \sin \theta_W, \quad (2.4)$$

146 with the usual definitions of the electroweak parameters:

$$\begin{aligned} \tan \theta_W &= \frac{g'}{g} \\ e &= \frac{gg'}{\sqrt{g^2 + g'^2}} \\ g &= e / \sin \theta_w \\ g' &= e / \cos \theta_w. \end{aligned} \quad (2.5)$$

147 The Z boson, on the other hand, mixes with the neutral component of the triplet, V^0 , with
 148 a rotation parametrized with the angle θ_N :

$$\begin{pmatrix} \cos \theta_N & \sin \theta_N \\ -\sin \theta_N & \cos \theta_N \end{pmatrix} \begin{pmatrix} Z \\ V^0 \end{pmatrix}. \quad (2.6)$$

149 The mass matrix of the rotated system is given by:

$$\mathbb{M}_N^2 = \begin{pmatrix} \hat{m}_Z^2 & c_H \zeta \hat{m}_Z \hat{m}_V \\ c_H \zeta \hat{m}_Z \hat{m}_V & \hat{m}_V^2 \end{pmatrix}, \quad (2.7)$$

2.2 Heavy Vector Triplet

150 where the parameters are defined as:

$$\begin{cases} \hat{m}_Z = \frac{e}{2 \sin \theta_W \cos \theta_W} \hat{v} \\ \hat{m}_V^2 = m_V^2 + g_V^2 c_{VVHH} \hat{v}^2 \\ \zeta = \frac{g_V \hat{v}}{2 \hat{m}_V} \\ \frac{\hat{v}^2}{2} = \langle H^\dagger H \rangle \end{cases}, \quad (2.8)$$

151 and \hat{v} , the vacuum expectation value of the Higgs field, can be different from the SM $v = 246$
152 GeV. The physical masses of Z and V^0 , m_Z and M_0 , and θ_N come from the matrix relations:

$$\begin{aligned} \text{Tr}(\mathbb{M}_N^2) &= \hat{m}_Z^2 + \hat{m}_V^2 = m_Z^2 + M_0^2 \\ \|\mathbb{M}_N^2\| &= \hat{m}_Z^2 + \hat{m}_V^2 (1 - c_H^2 \zeta^2) = m_Z^2 M_0^2 \\ \tan 2\theta_N &= \frac{2c_H \zeta \hat{m}_Z \hat{m}_V}{\hat{m}_V^2 - \hat{m}_Z^2}. \end{aligned} \quad (2.9)$$

153 The W^\pm bosons mix with the charged components of the triplet, V^\pm , leading to a mass
154 matrix analogous to eq. 2.10:

$$\mathbb{M}_C^2 = \begin{pmatrix} \hat{m}_W^2 & c_H \zeta \hat{m}_W \hat{m}_V \\ c_H \zeta \hat{m}_W \hat{m}_V & \hat{m}_V^2 \end{pmatrix}, \quad (2.10)$$

155 where \hat{m}_W is defined as:

$$\begin{cases} \hat{m}_W = \frac{e}{2 \sin \theta_W} \hat{v} = \hat{m}_Z \cos \theta_W \end{cases}; \quad (2.11)$$

156 the physical masses of W and V^\pm , m_W and M_\pm , and the angle θ_C parametrizing the rotation
157 of the charged sector are described by:

$$\begin{aligned} \text{Tr}(\mathbb{M}_C^2) &= \hat{m}_W^2 + \hat{m}_V^2 = m_W^2 + M_\pm^2 \\ \|\mathbb{M}_C^2\| &= \hat{m}_W^2 + \hat{m}_V^2 (1 - c_H^2 \zeta^2) = m_W^2 M_\pm^2 \\ \tan 2\theta_C &= \frac{2c_H \zeta \hat{m}_W \hat{m}_V}{\hat{m}_V^2 - \hat{m}_W^2}. \end{aligned} \quad (2.12)$$

158 The custodial symmetry of eq. 2.3 guarantees that:

$$\mathbb{M}_C^2 = \begin{pmatrix} \cos \theta_W & 0 \\ 0 & 1 \end{pmatrix} \mathbb{M}_N^2 \begin{pmatrix} \cos \theta_W & 0 \\ 0 & 1 \end{pmatrix}. \quad (2.13)$$

159

160 By taking the determinant of these matrices, a custodial relation among the masses can be
161 extracted:

$$m_W^2 M_\pm^2 = \cos \theta_W m_Z^2 M_0^2, \quad (2.14)$$

162 that has some very important consequences.

163 Given that this model aims at searching new particles in the TeV scale and that the scale of
164 the electroweak interactions must lay at ~ 100 GeV, a hierarchy of the physical masses seems
165 very natural:

$$\frac{\hat{m}_{(W,Z)}}{\hat{m}_V} \sim \frac{m_{(W,Z)}}{M_{(\pm,0)}} \ll 1; \quad (2.15)$$

¹⁶⁶ ζ parameter can be $\zeta \ll 1$ (weakly coupled scenario) or $\zeta \sim 1$ (strongly coupled scenario).
¹⁶⁷ When eq. 2.15 applies, the second lines in eq. 2.9 and eq. 2.12 can be approximated as follows:

¹⁶⁸

$$\begin{aligned} m_Z^2 &= \hat{m}_Z^2 (1 - c_H^2 \zeta^2) (1 + \mathcal{O}(\hat{m}_Z^2 / \hat{m}_V^2)) \\ m_W^2 &= \hat{m}_W^2 (1 - c_H^2 \zeta^2) (1 + \mathcal{O}(\hat{m}_W^2 / \hat{m}_V^2)). \end{aligned} \quad (2.16)$$

¹⁶⁹
¹⁷⁰ From eq. 2.11, the ratio of the physical masses of the charged and neutral electroweak bosons
¹⁷¹ can be approximated as:

$$\frac{m_W^2}{m_Z^2} \approx \cos \theta_W^2, \quad (2.17)$$

¹⁷² that satisfies the SM tree-level relation $\rho = 1$ if $\cos \theta_W^2 \approx 1 - 0.23$. Adding this approximation
¹⁷³ into eq. 2.14, the V bosons are expected to have the same masses, hence the same production
¹⁷⁴ rates:

$$M_{\pm}^2 = M_0^2 (1 + \mathcal{O}(%)). \quad (2.18)$$

¹⁷⁵ The degenerate mass of the triplet will be called $M_V \approx M_{\pm} \approx M_0$; given 2.15, $M_V = \hat{m}_V$.
¹⁷⁶ Another consequence of the mass hierarchy (2.15) is that the mixing angles $\theta_{(N,C)}$ between the
¹⁷⁷ electroweak fields and the triplet are small:

$$\theta_{(N,C)} \approx c_H \zeta \frac{\hat{m}_{(W,Z)}}{\hat{m}_V} \ll 1, \quad (2.19)$$

¹⁷⁸ hence the couplings among SM particles are very close to the couplings predicted by the SM.

¹⁷⁹ 2.2.2.1 Decay widths into fermions

¹⁸⁰ The couplings among the triplet and SM fermions are expressed as a function of the rotation
¹⁸¹ angles $\theta_{(C,N)}$ and SM couplings (omitting the CKM matrix elements for quarks):

$$\begin{cases} g_L^N = \frac{g^2}{g_V^2} \frac{c_F}{2} \cos \theta_N + (g_L^Z)_{SM} \sin \theta_N \approx \frac{g^2}{g_V^2} \frac{c_F}{2}, \\ g_R^N = (g_R^Z)_{SM} \sin \theta_N \approx 0 \\ g_L^C = \frac{g^2}{g_V^2} \frac{c_F}{2} \cos \theta_C + (g_L^W)_{SM} \sin \theta_N \approx \frac{g^2}{g_V^2} \frac{c_F}{2}, \\ g_R^C = 0 \end{cases}, \quad (2.20)$$

¹⁸² where $g_L^W = g/\sqrt{2}$; $g_{L,R}^{W,Z}$ are those predicted by the standard model. The V bosons interact
¹⁸³ with SM left fermions, and the strength of the couplings with fermions is determined by
¹⁸⁴ $g^2/g_V c_F$, as stated in sec. 2.2.1. The decay width into fermions is then given by:

$$\Gamma_{V^{\pm} \rightarrow f\bar{f}} \approx 2\Gamma_{V^0 \rightarrow f\bar{f}} \approx N_c \left(\frac{g^2 c_F}{g_V} \right)^2 \frac{M_V}{48\pi}, \quad (2.21)$$

¹⁸⁵ where N_c is the number of colours (3 for quarks, 1 for leptons).

2.2 Heavy Vector Triplet

186 2.2.2.2 Decay widths into bosons

187 As a starting point, a proper choice of the gauge makes the derivation of the approximate
 188 decay widths easier. While the unitary gauge is very convenient in discussing the electroweak
 189 symmetry breaking mechanism, since it provides a basis in which the Goldstone components
 190 of the scalar fields of the theory are set to zero, it does not properly describe the longitudinally
 191 polarized bosons in high-energy regimes, since it introduces a dependence of the type E/m in
 192 the longitudinal polarization vector, not corresponding to the experimental results. This patho-
 193 logical behaviour can be overcome profiting of the equivalence theorem: while calculating
 194 the scattering amplitude of an high-energy process, the longitudinally polarized vectors are
 195 equivalent to their corresponding Goldstone scalars. The scattering amplitude can therefore
 196 be calculated with Goldstone diagrams.

197 In the so-called equivalent gauge [15], the Higgs doublet is then parametrized as:

$$H = \begin{pmatrix} i\pi_+ \\ \frac{h+h-i\pi_0}{\sqrt{2}} \end{pmatrix}, \quad (2.22)$$

198 and the Goldstones π_0 and π_+ describe respectively W and Z longitudinal bosons; h is the
 199 physical Higgs boson. Rewriting the simplified Lagrangian 2.3 with 2.22 parametrization,
 200 two terms hold the information of the interaction of the V s with the Goldstones:

$$\mathcal{L}_\pi = \dots + c_H \zeta \hat{m}_V V_\mu^a \partial^\mu \pi^a + \frac{g_V c_H}{2} V_\mu^a \left(\partial^\mu h \pi^a - h \partial^\mu \pi^a + \epsilon^{abc} \pi^b \partial^\mu \pi^c \right) + \dots, \quad (2.23)$$

201 that are ruled by the $c_H g_V$ parameters combination. When ζ parameter is $\zeta \approx 1$, the first term
 202 in eq. 2.23 becomes important, and it is absorbed by a redefinition of the V_μ^a and π^a fields,

$$\begin{aligned} V_\mu^a &\rightarrow V_\mu^a + \frac{c_H \zeta}{\hat{m}_V} \partial_\mu \pi^a \\ \pi^a &\rightarrow \frac{1}{\sqrt{1 - c_H^2 \zeta^2}} \pi^a; \quad c_H^2 \zeta^2 < 1. \end{aligned} \quad (2.24)$$

203 By properly taking into account all the terms of the simplified lagrangian in the equivalent
 204 gauge, the partial widths of the dibosonic decays are ($\hat{m}_V = M_V$):

$$\begin{aligned} \Gamma_{V^0 \rightarrow W_L^+ W_L^-} &\approx \Gamma_{V^\pm \rightarrow W_L^\pm Z_L} \approx \frac{g_V^2 c_H^2 M_V}{192\pi} \frac{(1 + c_H c_{VVV} \zeta^2)^2}{(1 - c_H^2 \zeta^2)^2} = \frac{g_V^2 c_H^2 M_V}{192\pi} (1 + \mathcal{O}(\zeta^2)) \\ \Gamma_{V^0 \rightarrow Z_L h} &\approx \Gamma_{V^\pm \rightarrow W_L^\pm h} \approx \frac{g_V^2 c_H^2 M_V}{192\pi} \frac{(1 - 4c_H c_{VVV} \zeta^2)^2}{(1 - c_H^2 \zeta^2)^2} = \frac{g_V^2 c_H^2 M_V}{192\pi} (1 + \mathcal{O}(\zeta^2)). \end{aligned} \quad (2.25)$$

205 2.2.2.3 Decays in fermions and bosons: concluding remarks

206 From eq. 2.21-2.25, some important conclusions can be extracted.

- 207 • When ζ parameter is small, all the triplet decays (both in fermions and in dibosons),
 208 branching fractions and productions are completely determined by $g^2 c_F / g_V$, $g_V c_H$, and
 209 the degenerate mass of the triplet M_V ,
- 210 • c_{VVV} , c_{VVHH} , c_{VWW} can be neglected, as long as the interest is focused in narrow reso-
 211 nances.

2.2.3 HVT production

Given the mass scale of the resonances, the production mechanisms expected to be relevant are Drell-Yan (fig. 2.1) and Vector Boson Fusion (VBF) (fig. 2.2).

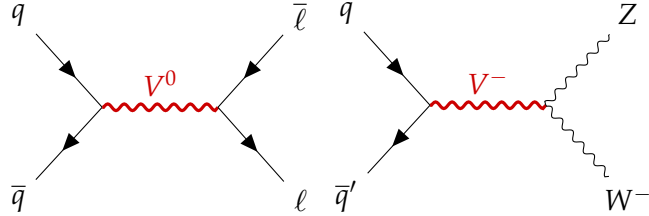


Figure 2.1: Examples of Drell-Yan production mechanism of a heavy V HVT boson: $q - \bar{q}$ quark scattering producing a neutral V^0 that decays leptonically (left); $q - \bar{q}'$ scattering producing a charged V^- that decays in a W and Z bosons (right).

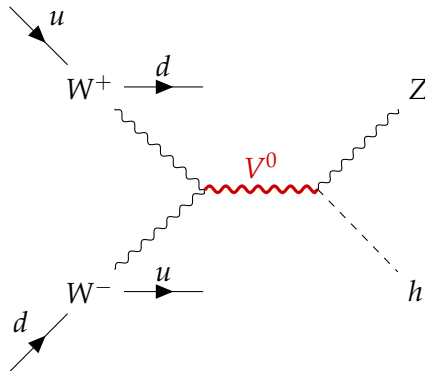


Figure 2.2: Example of VBF production mechanism of a heavy V HVT boson: a neutral V^0 boson is produced by a couple of W bosons, as a result of electroweak interactions of initial state u and d quarks. V^0 decays in a Z boson and a Higgs boson. The final state signature includes the presence of a pair of quarks, due to the primary interactions.

The cross-section of the production mechanisms is given by:

$$\sigma(pp \rightarrow V + X) = \sum_{i,j \in p} \frac{\Gamma_{V \rightarrow ij}}{M_V} f(J, S_i, S_j) g(C_i, C_j) \left. \frac{dL_{ij}}{ds} \right|_{s=M_V^2}, \quad (2.26)$$

where i, j are the partons involved in the hard interaction, Γ_{ij} is the partial width of the process $V \rightarrow ij$, $f(J, S_i, S_j)$ is a function of the spin of the resonance and of the partons, $g(C_i, C_j)$ is a function of the colour factors of each parton, s is the center-of-mass energy and $\frac{dL_{ij}}{ds}$ are the parton luminosities, that are independent from HVT model (that enters only in Γ_{ij}).

Parton luminosities, calculated for a center-of-mass energy of 14 TeV starting from quark and antiquark parton distribution functions (PDF), are displayed in fig. 2.3 (Drell-Yan mechanism) and 2.4 (VBF mechanism). VBF luminosities are suppressed by the α_{EW} factor, therefore the process is relevant only when the bosonic decays of the triplet are dominant (strongly coupled scenario).

2.2 Heavy Vector Triplet

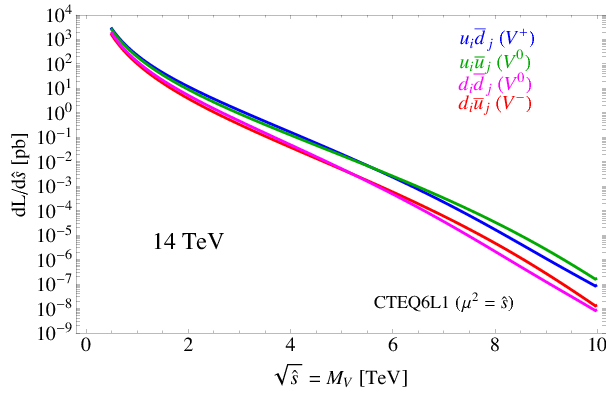


Figure 2.3: Parton luminosities for Drell-Yan process between i and j partons, as a function of the parton center-of-mass energy, for the LHC proton-proton collisions performed at 14 TeV.

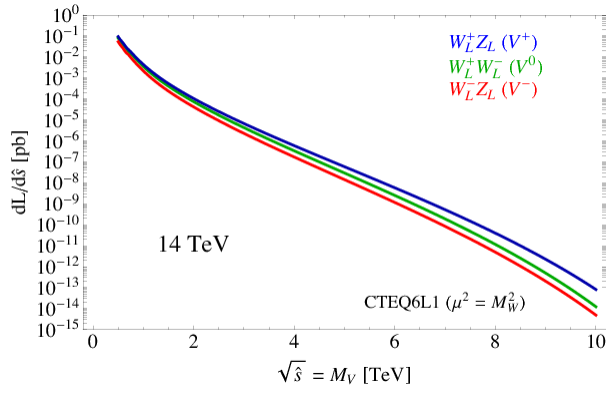


Figure 2.4: Parton luminosities for VBF process between i and j partons, as a function of the parton center-of-mass energy, for the LHC proton-proton collisions performed at 14 TeV.

225 **2.2.4 Benchmark model A: weak coupling scenario**

226 Model A scenario aims at reproducing a simple generalization of the SM [10], obtained by ex-
227 tending the gauge symmetry group with an additional $SU(2)'$. The low-energy phenomena
228 are expected to be dominated by the SM, while the high-energy processes are relevant for the
229 additional symmetry, bringing additional light vector bosons in play.
230 It can be shown that this kind of picture is portrayed by HVT when $c_H \sim -g^2/g_V^2$ and $c_F \sim 1$.
231 This implies that:

$$\begin{aligned} g_V c_H &\approx g^2/g_V \\ g^2 c_F/g_V &\approx g^2/g_V, \end{aligned} \tag{2.27}$$

232 hence the partial decay widths into fermions (eq. 2.21) and bosons (eq. 2.25) differ only by a
233 factor 2 and the colour factor (N_c). Branching fractions for the model A benchmark scenario
234 ($g_V = 1$) are shown in fig. 2.5 (left); total widths are reported in fig. 2.5 (right) for different
235 coupling parameters g_V .

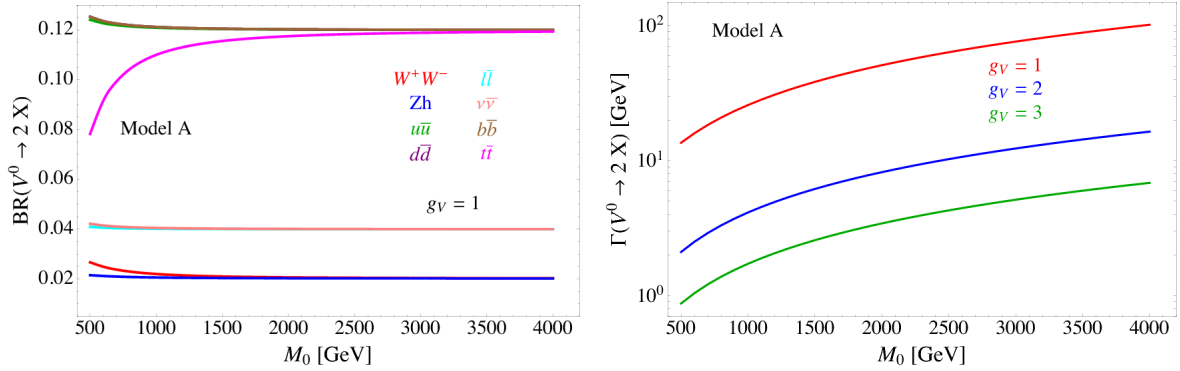


Figure 2.5: HVT model A scenario: branching fractions for fermionic and bosonic decays when $g_V = 1$ (left) as a function of the mass of the resonance M_0 ; total width of the resonance, as a function of its mass, considering different values of the parameter g_V (right).

2.2.5 Benchmark model B: strong coupling scenario

In composite Higgs models [12], the Higgs boson is the result of the spontaneous symmetry breaking of an $SO(5)$ symmetry to a $SO(4)$ group. New vector bosons are expected to appear, and the lightest ones can be represented by HVT model B when $c_H \sim c_F \sim 1$.

In this case:

$$\begin{aligned} g_V c_H &\approx -g_V \\ g^2 c_F / g_V &\approx g^2 / g_V, \end{aligned} \quad (2.28)$$

hence the decay into bosons is not suppressed by g_V parameter. In the benchmark scenario $g_V = 3$, decays into dibosons are largely dominant, as it can be seen in fig. 2.6 (left); the total decay width increases for larger g_V (fig. 2.6, right). When the resonances start to be very broad, *i.e.* $\Gamma / M_V \gg 0.1$, the assumptions leading to the simplified model are no longer valid, hence higher order, non-resonant effects must be taken into account.

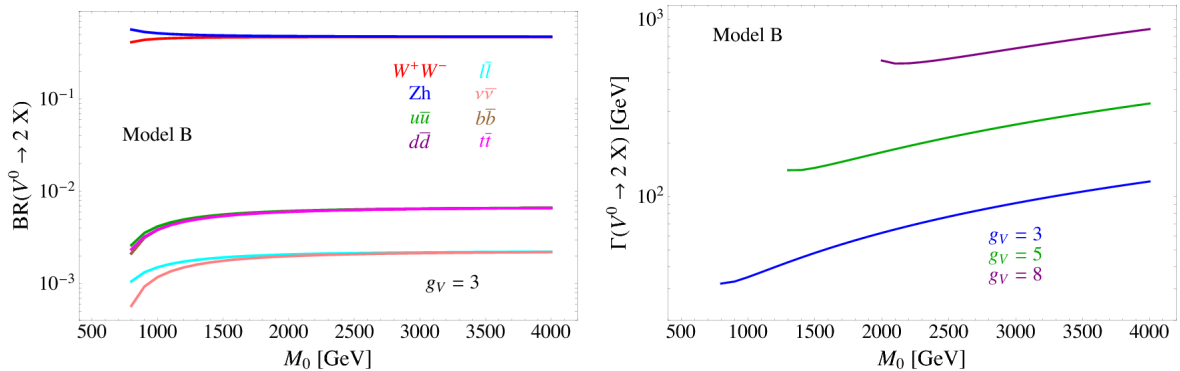


Figure 2.6: HVT model B scenario: branching fractions for fermionic and bosonic decays when $g_V = 3$ (left) as a function of the mass of the resonance M_0 ; total width of the resonance, as a function of its mass, considering different values of the parameter g_V (right).

2.2 Heavy Vector Triplet

2.2.6 Search for HVT resonances at LHC

No evidence of HVT resonances has been observed so far at LHC experiments. Data collected by ATLAS and CMS detectors are used to set limits on the HVT resonance masses and coupling parameters. Experimental results from proton-proton collisions performed at a center-of-mass energy of 8 TeV (Run 1 era) at LHC brought to the following conclusions. A weakly coupled resonance, in the context of benchmark model A ($g_V = 1$) was excluded up to 3 TeV by Run 1 data. By looking at parton luminosities in fig.2.3, in data produced by LHC proton-proton collision at 14 TeV, collected for an integrated luminosity of 300 fb^{-1} , the sensitivity is expected to increase up to $m_V \approx 6 \text{ TeV}$. A strongly coupled resonance, in the context of benchmark model B ($g_V = 3$) is excluded up to 2 TeV by Run 1 data. Data produced by LHC at 14 TeV should increase the sensitivity up to $m_V \approx 3 - 4 \text{ TeV}$. The most stringent limits are provided by the latest data produced by LHC at a center-of-mass energy of 13 TeV (Run 2 era).

Numerous searches for HVT triplet have been performed at CMS experiment in different final states: the most sensitive ones were those in all-hadronic topology. [16, 17] (search for WW , WZ , ZZ resonances in the $q\bar{q}q\bar{q}$ final state) excludes a W' with mass below 3.6 and a Z' with mass below 2.7 TeV in the model B scenario (fig. 2.7). [18, 19] (search for WH , ZH resonances in the $q\bar{q}b\bar{b}$ final state) excludes a W' lighter than 2.97 (3.15) TeV in the HVT model A (model B), and a Z' up to 1.67 (2.26) TeV in HVT model A (model B) (fig. 2.8). In fig. 2.9, results of [16, 17] (left) and [18, 19] (right) searches are interpreted as exclusion contours in the coupling parameter plane of the HVT model ($g_V c_H$ and $g^2 c_F / g_V$). In the grey shaded area, the narrow width approximation fails. The colored curves display the parameter exclusion for different mass hypotheses of the triplet. Colored dots show the model A and B benchmark scenarios.

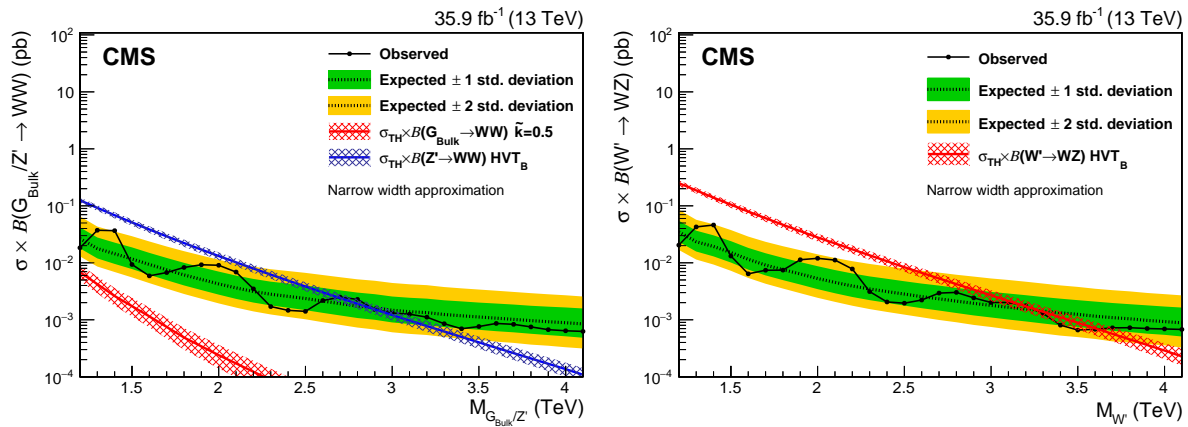


Figure 2.7: The observed and expected limits, with 68% and 95% uncertainty bands, on the product of the cross section and branching fraction $\sigma \mathcal{B}(Z' \rightarrow WW)$ for a spin-1 Z' (left) and $\sigma \mathcal{B}(W' \rightarrow WZ)$ for a spin-1 W' (right), as a function of the reconstructed mass of the diboson resonance. The colored lines show the theoretical predictions for the HVT model B.

Many other final states have been exploited at CMS: $ZW, ZZ \rightarrow \ell\bar{\ell}q\bar{q}$ [20]; $WH, ZH \rightarrow (\ell\bar{\ell}, \ell\nu, \nu\bar{\nu})b\bar{b}$ [21]; $WZ, WW \rightarrow \ell\nu q\bar{q}$ [22]. Finally, $ZW, ZZ \rightarrow \nu\bar{\nu}q\bar{q}$ [23] results will be extensively described in this thesis.

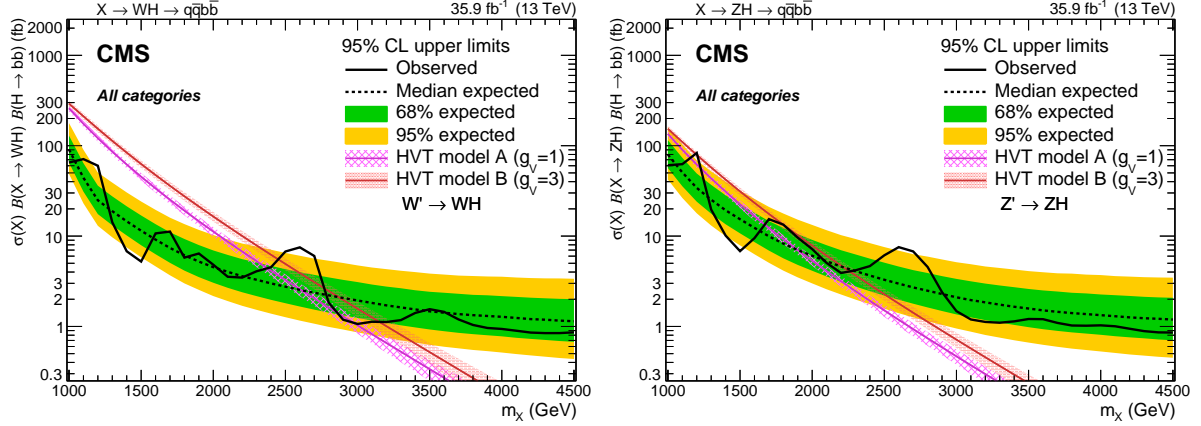


Figure 2.8: The observed and expected limits, with 68% and 95% uncertainty bands, on the product of the cross section and branching fraction $\sigma\mathcal{B}(W' \rightarrow WH)$ for a spin-1 W' (left) and $\sigma\mathcal{B}(Z' \rightarrow ZH)$ for a spin-1 Z' (right), as a function of the reconstructed mass of the diboson resonance. The colored lines show the theoretical predictions for the HVT model A and B.

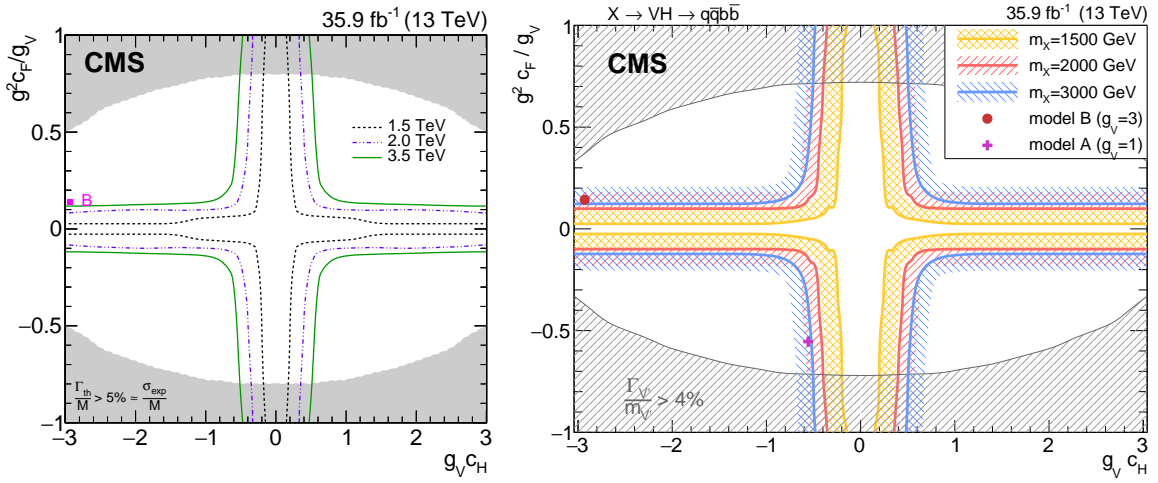


Figure 2.9: Exclusion contours in the coupling parameter plane of the HVT model ($g_V c_H$ and $g^2 c_F / g_V$).

2.2 Heavy Vector Triplet

273 Searches for HVT model B resonances have been performed at ATLAS experiment as well.
 274 Results for a $W' \rightarrow WZ$ reported in fig. 2.10 include the searches performed in $WW, WZ, ZZ \rightarrow$
 275 $q\bar{q}q\bar{q}$ final state [24]; $WZ, WW \rightarrow \ell\nu q\bar{q}$ final state [25]; $ZW, ZZ \rightarrow (\ell\bar{\ell}, \ell\nu, \nu\bar{\nu})q\bar{q}$ final state [26].
 276 The all-hadronic final state has the best sensitivity and it excludes a W' resonance up to 3.3
 277 TeV (model B scenario). Results for a $W' \rightarrow WH$ and for a $Z' \rightarrow ZH$ are displayed in fig. 2.11
 278 (left and right respectively), and they include searches performed in $WH, ZH \rightarrow qqb\bar{b}$ final
 279 state [27], and $WH, ZH \rightarrow \ell\bar{\ell}, \ell\nu, \nu\bar{\nu} b\bar{b}$ [28]. A W' is excluded up to 2.9 TeV and a Z' is
 280 excluded up to 2.8 TeV (in the model B scenario).

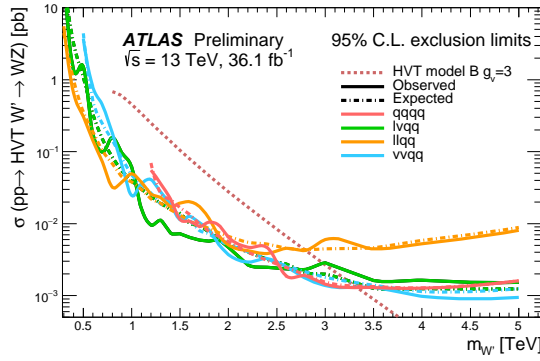


Figure 2.10: The observed and expected limits on the product of the cross section and branching fraction $\sigma\mathcal{B}(W' \rightarrow WZ)$ for a spin-1 W' , as a function of the reconstructed mass of the diboson resonance. The dotted line shows the theoretical predictions for the HVT model B.

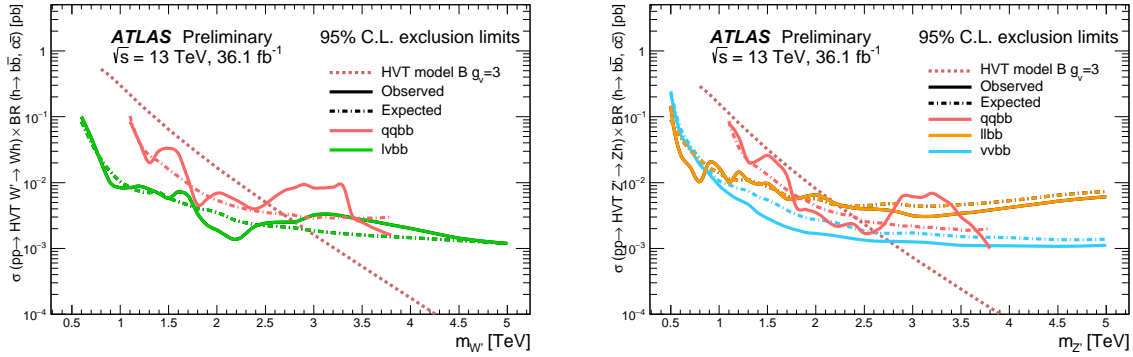


Figure 2.11: The observed and expected limits on the product of the cross section and branching fraction $\sigma\mathcal{B}(W' \rightarrow WH)$ for a spin-1 W' (left) and $\sigma\mathcal{B}(Z' \rightarrow ZH)$ for a spin-1 Z' (right), as a function of the reconstructed mass of the diboson resonance. The colored lines show the theoretical predictions for the HVT model B.

²⁸¹ **2.3 Warped extra dimension**

²⁸² The Randall-Sundrum model [29,30] (RS1) proposes the introduction of one additional warped
 283 dimension in order to solve the hierarchy problem. The metric of the 5-dimensional space (a
 284 slice of AdS_5) generates an exponential hierarchy between the electroweak and Planck scales,
 285 associated respectively to the TeV three-brane, where the SM particles are confined, and the
 286 Planck three-brane. As a consequence of the new geometry, spin-2 massive gravitons are pre-
 287 dicted to exist.

²⁸⁸ The bulk extension of the Randall-Sundrum model [31,32] states that the SM fields can prop-
 289 agate in the extra dimension. Light fermions are near the Planck brane, heavy fermions are
 290 close to the TeV brane, while the Higgs sector is confined in the TeV brane. Higgs couplings
 291 to the heavy fermions are therefore expected to be stronger: this naturally arising hierarchy
 292 of the masses of the SM fields gives a solution to the flavour problem. In this scenario, the
 293 fermionic decays of the bulk gravitons are suppressed, while the bosonic decays are preferred.

²⁹⁴ **2.3.1 Randall-Sundrum original model (RS1)**

²⁹⁵ The existence of additional n -dimensions implies that the effective Planck scale observed in
 296 4-dimensions, $M_{PL} = 1.220910^{19}$ GeV, is related to the fundamental $4+n$ -dimensional Planck
 297 scale, M , via the geometry. M is expected to be of the order of the reduced $\overline{M}_{PL} = M_{PL}/2\pi$.
 298 If the 4-dimensional and the n additional metrics are factorizable, \overline{M}_{PL} is the product of M
 299 and the volume of the compact space V_n :

$$\overline{M}_{PL}^2 = V_n M^{2+n}. \quad (2.29)$$

³⁰⁰ If $M \sim$ TeV, this implies that V_n must be very large, hence the compactification scale $\mu \sim 1/V_n^{1/n}$
 301 is small (eV – MeV for n=2 – 7). Given the smallness of μ when compared to the electroweak
 302 scale, the effects of the extra dimensions should be evident in SM processes. Since they are
 303 not observed, SM particles are assumed to be confined in a 4-dimensional space, the TeV
 304 three-brane, while only gravity is allowed to propagate into the $4+n$ -dimensional space, the
 305 bulk. This mechanism solves the hierarchy of the Higgs scale but introduces a new hierarchy
 306 between μ and M .

³⁰⁷ In the Randall-Sundrum model [29, 30], only one additional dimension is added. The ge-
 308 ometry of the 5-dimensional bulk is non-factorizable, and it is a slice of AdS_5 spacetime.¹
 309 The 4-dimensional metric is multiplied by an exponential function of the fifth dimension (the
 310 "warp" factor):

$$ds^2 = e^{-2kr_c\phi} \eta_{\mu\nu} dx^\mu dx^\nu + r_c^2 d\phi^2; \quad (2.30)$$

³¹¹ x^μ are the usual 4-dimensional coordinates, $\eta_{\mu\nu} = diag(-1, 1, 1, 1)$ is the Minkowski metric, k
 312 is a scale of order of \overline{M}_{PL} , ϕ is the coordinate of the extra dimension, $0 < |\phi| < \pi$, and r_c is
 313 the compactification radius of this finite interval. 4-dimensional mass scales are obtained by
 314 multiplying the bulk masses by $e^{-2kr_c\phi}$: given the exponential form of the warp factor, a small
 315 r_c suffices for generating a large hierarchy between Planck and Higgs scales.

³¹⁶ Two 4-dimensional three-branes are located at the boundaries of the fifth dimension: the
 317 visible brane at $\phi = \pi$; the hidden brane at $\phi = 0$, and their metrics are obtained starting from

¹An n -dimensional anti-de Sitter space (AdS_n) is a maximally symmetric Lorentzian manifold, that solves the Einstein equation with a negative curvature (negative cosmological constant).

2.3 Warped extra dimension

³¹⁸ the bulk 5-dimensional metric G_{MN} , where $M, N = \mu, \phi$:

$$\begin{aligned} g_{\mu\nu}^{\text{vis}}(x^\mu) &= G_{\mu\nu}(x^\mu, \phi = \pi) \\ g_{\mu\nu}^{\text{hid}}(x^\mu) &= G_{\mu\nu}(x^\mu, \phi = 0). \end{aligned} \quad (2.31)$$

³¹⁹ The classical action is given by:

$$\begin{aligned} S &= S_{\text{gravity}} + S_{\text{vis}} + S_{\text{hid}} \\ S_{\text{gravity}} &= \int d^4x \int_{-\pi}^{+\pi} d\phi \sqrt{-G} (-\Lambda + 2M^3\mathcal{R}) \\ S_{\text{vis}} &= \int d^4x \sqrt{-g_{\text{vis}}} (\mathcal{L}_{\text{vis}} - V_{\text{vis}}) \\ S_{\text{hid}} &= \int d^4x \sqrt{-g_{\text{hid}}} (\mathcal{L}_{\text{hid}} - V_{\text{hid}}), \end{aligned} \quad (2.32)$$

³²⁰ where G (g) is the trace of the G_{MN} ($g_{\mu\nu}$) metric, Λ is the cosmological constant in the bulk,
³²¹ \mathcal{R} is the 5-dimensional Ricci scalar, \mathcal{L} and V are the lagrangian and the vacuum energy of the
³²² hidden and visible branes.

³²³ A 5-dimensional metric that preserves the 4-dimensional Poincaré invariance has the form:

$$ds^2 = e^{-2\sigma(\phi)} \eta_{\mu\nu} dx^\mu dx^\nu + r_c^2 d\phi^2. \quad (2.33)$$

³²⁴ The Poincaré invariance guarantees that r_c does not depend on x^μ . Given 2.33, the solution of
³²⁵ the 5-dimensional Einstein's equations simplifies into:

$$\sigma = r_c |\phi| \sqrt{\frac{-\Lambda}{24M^3}}. \quad (2.34)$$

³²⁶ Furthermore, the Poincaré invariance imposes constraints to the vacuum energies and cosmo-
³²⁷ logical constant:

$$\begin{aligned} V_{\text{hid}} &= -V_{\text{vis}} = 24M^3k \\ \Lambda &= -24M^3k^2. \end{aligned} \quad (2.35)$$

³²⁸ The final 5-dimensional metric is then:

$$ds^2 = e^{-2kr_c|\phi|} \eta_{\mu\nu} dx^\mu dx^\nu + r_c^2 d\phi^2. \quad (2.36)$$

³²⁹ A small r_c is considered, so the effects of the fifth dimension on 4-dimensional spacetime
³³⁰ can't be appreciated. A 4-dimensional effective field theory approach is therefore motivated,
³³¹ and its mass parameters are related to the bulk parameters, M , k and r_c . In the Randall-
³³² Sundrum model, SM matter fields are confined in the TeV brane.

³³³ The massless gravitons, the mediators of the gravitational interaction in the effective field
³³⁴ theory, are the zero modes ($h_{\mu\nu}$) of the quantum fluctuations of the classical solution (2.36):

$$ds^2 = e^{-2kT(x)|\phi|} (\eta_{\mu\nu} + h_{\mu\nu}(x)) dx^\mu dx^\nu + T^2(x) d\phi^2, \quad (2.37)$$

³³⁵ where the usual Minkowski metric has been replaced by $\bar{g}_{\mu\nu}(x) = \eta_{\mu\nu} + h_{\mu\nu}$; $h_{\mu\nu}$ are the
³³⁶ tensor fluctuations around the Minkowski space, and represent both the physical graviton in
³³⁷ 4-dimensions and the massless mode of the Kaluza-Klein decomposition of the bulk metric.

³³⁸ r_c is the vacuum expectation value of $T(x)$.

³³⁹ By substituting eq. 2.37 in the classical action 2.32, an effective action can be extracted, and in
³⁴⁰ particular the curvature term holds:

$$S_{\text{eff}} \sim \int d^4x \int_{-\pi}^{+\pi} d\phi 2M^3 r_c e^{-2kr_c|\phi|} \bar{\mathcal{R}} \sqrt{-\bar{g}}, \quad (2.38)$$

³⁴¹ where \bar{g} is the trace of $\bar{g}_{\mu\nu}$ and $\bar{\mathcal{R}}$ is the 4-dimensional Ricci scalar of $\bar{g}_{\mu\nu}$ metric. In this
³⁴² effective 4-dimensional action, the ϕ dependence can be integrated out, and the 4-dimensional
³⁴³ Planck mass can be calculated:

$$\bar{M}_{PL}^2 = M^3 r_c \int_{-\pi}^{+\pi} d\phi e^{-2kr_c|\phi|} = \frac{M^3}{k} \left(1 - e^{-2kr_c\pi}\right). \quad (2.39)$$

³⁴⁴ It can be shown [29] that a field with a fundamental mass parameter m_0 in the bulk manifests
³⁴⁵ in the visible three-brane with a physical mass m :

$$m = e^{-2kr_c\pi} m_0. \quad (2.40)$$

³⁴⁶ Scales $m \sim \text{TeV}$ are generated from $m_0 \sim \bar{M}_{PL}$ if $e^{kr_c\pi} \sim 10^{15}$. This relation stands still when
³⁴⁷ Higgs field is introduced and confined in the visible three-brane:

$$v = e^{-2kr_c\pi} v_0, \quad (2.41)$$

³⁴⁸ where v is the Higgs vacuum expectation value in the TeV brane and v_0 is the 5-dimensional
³⁴⁹ Higgs v.e.v.

³⁵⁰ The hierarchy problem is then solved by the exponential warp factor. The weakness of gravity
³⁵¹ in the TeV three-brane is motivated by the small overlap of the graviton wave function.

³⁵² In order to calculate the mass spectrum of the graviton in the TeV brane, the tensor fluctuations
³⁵³ of the Minkowski metric are expanded into a Kaluza-Klein (KK) tower $h_{\mu\nu}^{(n)}$:

$$h_{\mu\nu}(x, \phi) = \sum_{n=0}^{\infty} h_{\mu\nu}^{(n)}(x) \frac{\chi^{(n)}(\phi)}{\sqrt{r_c}}. \quad (2.42)$$

³⁵⁴ Once a suitable gauge is chosen, i.e. $\eta^{\mu\nu} \partial_\mu h_{\nu\alpha}^{(n)} = \eta^{\mu\nu} h_{\mu\nu}^{(n)} = 0$, the equation of motion of $h_{\mu\nu}^{(n)}$
³⁵⁵ becomes the Klein-Gordon relation, where $m_n^G \geq 0$:

$$\left(\eta^{\mu\nu} \partial_\mu \partial_\nu - (m_n^G)^2 \right) h_{\mu\nu}^{(n)}(x) = 0. \quad (2.43)$$

³⁵⁶ By substituting eq. 2.42 into Einstein's equation, the solutions for $\chi^{(n)}(\phi)$ (commonly called
³⁵⁷ "profiles") are [33,34]:

$$\chi^{(n)}(\phi) = \frac{e^{2\sigma}}{N} \left[J_2(z_n^G) + \alpha_n Y_2(z_n^G) \right], \quad (2.44)$$

³⁵⁸ where J_2 and Y_2 are second order Bessel functions, N is the normalization of the wavefunction,
³⁵⁹ α_n are coefficients and $z_n^G = m_n^G e^{\sigma(\phi)}/k$. m_n^G is the mass of the n -mode, and it depends on the
³⁶⁰ roots of the Bessel functions $z_n^G = (3.83, 7.02, 10.17, 13.32, \dots)$. In the limit $m_n^G/k \ll 1$ and
³⁶¹ $e^{kr_c\pi} \gg 1$:

$$m_n^G = k z_n^G(\pi) e^{-kr_c\pi}. \quad (2.45)$$

2.3 Warped extra dimension

362 The interactions between the graviton KK modes and the matter fields in the TeV brane can be
363 derived from the 4-dimensional effective Lagrangian, once $h_{\mu\nu}$ is replaced by its KK decom-
364 position:

$$\mathcal{L} = -\frac{1}{M_{PL}} T^{\mu\nu}(x) h_{\mu\nu}^{(0)} - \frac{1}{e^{-kr_c\pi} M_{PL}} T^{\mu\nu}(x) \sum_{n=1}^{\infty} h_{\mu\nu}^{(n)}(x); \quad (2.46)$$

365 $T^{\mu\nu}$ is the space energy-momentum tensor of the matter fields. The zero mode of the gravitons
366 coupling is $1/M_{PL}$, while higher order KK modes couplings to all SM fields are suppressed
367 by $e^{-kr_c\pi} M_{PL}$, that is of the order of the TeV scale. Spin-2 KK masses and couplings are hence
368 determined by the TeV scale, or, equivalently, KK gravitons are close to the TeV brane. This
369 implies that KK gravitons can be produced via $q\bar{q}$ or gluon fusion, and that a leptonic decay
370 of the resonance could represent a very clear signal signature.

371 2.3.2 Bulk extension of RS1: graviton production and decays

372 An extension of the original RS1 formulation has been proposed. It states that the usual SM
373 fields are no longer confined in the TeV brane, but they are the zero modes of the correspond-
374 ing 5-dimensional SM fields. If first and second generation fermions are close to the Planck
375 brane, contribution to flavour changing neutral currents by higher-dimensional operators are
376 suppressed. These contributions are excluded by electroweak precision tests, but they were
377 not prevented in original RS1. The second motivation behind the choice is, as mentioned pre-
378 viously, the naturally arising flavour hierarchy: first and second generation quarks have small
379 Yukawa couplings to the Higgs sector, confined in the TeV brane, while top quark and bosons
380 have stronger Yukawa couplings.

381 In this picture, couplings between higher-order KK gravitons and light fermions are strongly
382 suppressed, resulting into a negligible KK gravitons production via $q\bar{q}$, whilst gluon fusion
383 production becomes dominant. KK gravitons decay into top quarks and Higgs bosons are
384 dominant, given that both their profiles are near the TeV brane, while leptonic decays are
385 negligible. Via the equivalence theorem, the Goldstone bosons are equivalent to the longitu-
386 dinally polarized weak bosons, W_L^\pm and Z_L , that have profiles close to the TeV brane. Decays
387 of KK gravitons into weak dibosons (and production in VBF) are comparable to di-top and
388 di-Higgs decays.

389

390 The KK decomposition and the KK mass spectrum of the graviton have already been pre-
391 sented in sec. 2.3.1. The KK decomposition of a massless 5-dimensional gauge field $A_M(x, \phi)$
392 is similarly performed [35]:

$$A_\mu(x, \phi) = \sum_{n=0}^{\infty} A_\mu^{(n)}(x) \frac{\chi_A^{(n)}(\phi)}{\sqrt{r_c}}. \quad (2.47)$$

393 The profiles for the gauge fields are:

$$\chi_A^{(n)}(\phi) = \frac{e^\sigma}{N_A} \left[J_1(z_n^A) + \alpha_n^A Y_1(z_n^A) \right], \quad (2.48)$$

394 where J_1 and Y_1 are first order Bessel functions. Similarly to eq. 2.49, the mass spectrum of
395 the gauge field is:

$$m_n^A = kz_n^A(\pi) e^{-kr_c\pi}; \quad (2.49)$$

³⁹⁶ the first roots of the Bessel functions are $z_n^A = (2.45, 5.57, 8.70, 11.84, \dots)$.

³⁹⁷ The Lagrangian expressing the interaction between the m and n modes of the bulk field F
³⁹⁸ to the q KK gravitons mode G is [35]:

$$\mathcal{L}_{G-F} = \sum_{m,n,q} C_{mnq}^{FFG} \frac{1}{M_{PL}} \eta^{\mu\alpha} \eta^{\nu\beta} h_{\alpha\beta}^{(q)}(x) T_{\mu\nu}^{(m,n)}(x), \quad (2.50)$$

³⁹⁹ C_{mnq}^{FFG} is the overlap integral of the profiles:

$$C_{mnq}^{FFG} = \int \frac{d\phi}{\sqrt{k}} e^{t\sigma} \chi_F^{(m)} \chi_F^{(n)} \chi_G^{(q)}; \quad (2.51)$$

⁴⁰⁰ t depends on the type of field considered.

⁴⁰¹ The coupling between gluons and the q KK graviton mode is given by:

$$C_{00q}^{AAG} = e^{k\pi r_c} \frac{2 [1 - J_0(x_n^G)]}{k\pi r_c (x_n^G)^2 |J_2(x_n^G)|}. \quad (2.52)$$

⁴⁰² Once eq. 2.52 is put in eq. 2.50, the most significant partial decay widths into the q KK graviton
⁴⁰³ mode are:

$$\begin{aligned} \Gamma(G \rightarrow t_R \bar{t}_R) &\sim N_c \frac{[\tilde{k} x_q^G]^2 m_q^G}{320\pi} \\ \Gamma(G \rightarrow hh) &\sim \frac{[\tilde{k} x_q^G]^2 m_q^G}{960\pi} \\ \Gamma(G \rightarrow W_L^+ W_L^-) &\sim \frac{[\tilde{k} x_q^G]^2 m_q^G}{480\pi} \\ \Gamma(G \rightarrow Z_L Z_L) &\sim \frac{[\tilde{k} x_q^G]^2 m_q^G}{960\pi}, \end{aligned} \quad (2.53)$$

⁴⁰⁴ where $\tilde{k} = k/\overline{M}_{PL}$; the total decay width is:

$$\Gamma_G = \frac{13 [\tilde{k} x_q^G]^2 m_q^G}{960\pi}. \quad (2.54)$$

⁴⁰⁵ Calculations, so far, have been performed considering $M \sim \overline{M}_{PL}$ and $k < M$, hypotheses
⁴⁰⁶ under which the solution for the bulk metric (eq. 2.36) is valid. Hence, $\tilde{k} = k/\overline{M}_{PL} \leq 1$ is
⁴⁰⁷ taken as a reference interval. This has also phenomenological consequences on the width of
⁴⁰⁸ the resonance, as stated in eq. 2.54. The total decay width of the lightest KK graviton mode,
⁴⁰⁹ compared to its mass, is shown as a function of \tilde{k} in fig. 2.12 [36]. At $\tilde{k} = 1$, in the bulk
⁴¹⁰ scenario, the KK graviton width is expected to be few % of its mass, up to 4 TeV (dotted red
⁴¹¹ curve). The narrow width approximation holds, hence the resonance properties can be probed
⁴¹² at the peak, neglecting the effects in the tails of the mass distribution.

⁴¹³ The total cross-section of a bulk graviton, produced at LHC in proton-proton interactions
⁴¹⁴ via gluon fusion (displayed in fig. 2.13), decaying into a couple of vector bosons (for the
⁴¹⁵ purpose of this thesis, a final state with two longitudinally polarized Z bosons is considered)

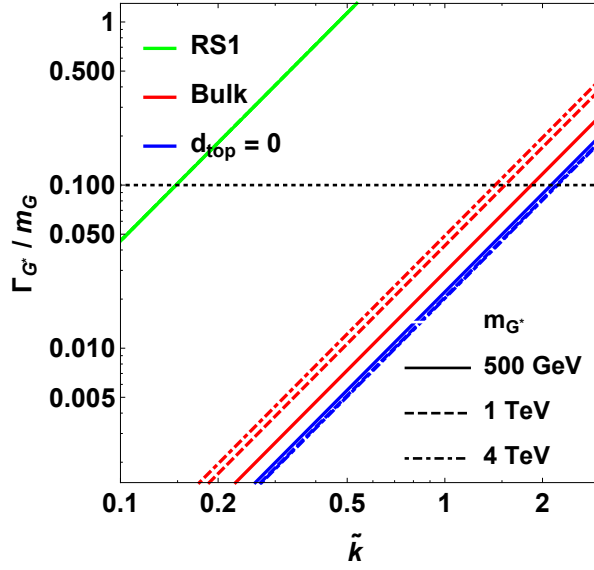


Figure 2.12: Width of the KK gravitons, in units of the mass of the resonance, as a function of the curvature parameter \tilde{k} . The red curves represent the bulk extension of RS1 original model for different mass hypotheses (from 500 GeV up to 4 TeV).

⁴¹⁶ is expressed as a function of the parton level cross-section $\hat{\sigma}$, the gluon parton distribution
⁴¹⁷ functions f_g , the momentum transfer $Q^2 \sim (m_q^G)^2$ and the center-of-mass energy s :

$$\sigma(pp \rightarrow ZZ) = \int dx_1 dx_2 f_g(x_1, Q^2) f_g(x_2, Q^2) \hat{\sigma}(x_1 x_2 s). \quad (2.55)$$

⁴¹⁸ The differential parton level cross-section, averaged over colors and initial spin states, is (hatted
⁴¹⁹ quantities are calculated in the center-of-mass frame):

$$\frac{d\hat{\sigma}(gg \rightarrow ZZ)}{d \cos \hat{\theta}} \approx \frac{|\mathcal{M}_{+-00}|^2}{1024\pi \hat{s}}, \quad (2.56)$$

⁴²⁰ where $|\mathcal{M}_{+-00}|$ is the matrix element of the dominant contribution in $gg \rightarrow VV$ process (Γ_G
⁴²¹ is defined in eq. 2.54, a, b are color factors):

$$\mathcal{M}_{+-00}(g^a g^b \rightarrow VV) = -C_{00q}^{AAG} e^{-k\pi r_c} \left(\frac{x_n^G \tilde{k}}{m_n^G} \right)^2 \sum_n \frac{\delta_{ab} \mathcal{A}_{+-00}}{\hat{s} - m_n^G{}^2 + i\Gamma_G m_n^G}. \quad (2.57)$$

⁴²² The relevant amplitudes taken account in the matrix element calculation are [31]:

$$\mathcal{A}_{+-00} = \mathcal{A}_{-+00} = \frac{(1 - 1/\beta_Z^2) (\beta_Z^2 - 2) [(t - \hat{u})^2 - \beta_Z^2 \hat{s}^2] \hat{s}}{8M_Z^2}, \quad (2.58)$$

⁴²³ where $\beta_Z^2 = 1 - 4M_Z^2/\hat{s}$ and M_Z is the mass of the Z boson.

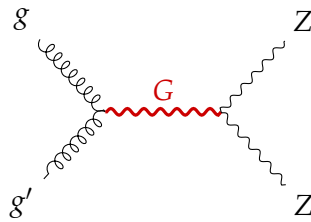


Figure 2.13: Gluon fusion production mechanism for a KK graviton that decays in a couple of Z bosons.

424 2.3.3 Search for KK bulk gravitons at LHC

425 No evidence of spin-2 bulk graviton resonances has been observed so far at LHC experiments.
 426 Data collected by ATLAS and CMS detectors are used to set limits on the graviton masses,
 427 generally considering different curvature parameter \tilde{k} hypotheses, once assured the narrow
 428 width approximation is still valid (up to $\tilde{k} \sim 1$). The most stringent limits have been set with
 429 Run 2 data.

430 Many results of the diboson searches performed at CMS and already presented in sec. 2.2.6
 431 are interpreted in the context of the bulk gravitons, together with the additional final states
 432 $WZ, ZZ \rightarrow \ell\bar{\nu}\ell\bar{\nu}$ [37] and $HH \rightarrow b\bar{b}b\bar{b}$ [38]. The most interesting limit is provided by [37], that,
 433 under the hypothesis $\tilde{k} = 0.5$, excludes a spin-2 bulk graviton with a mass lower than 800 GeV
 434 (fig. 2.14).

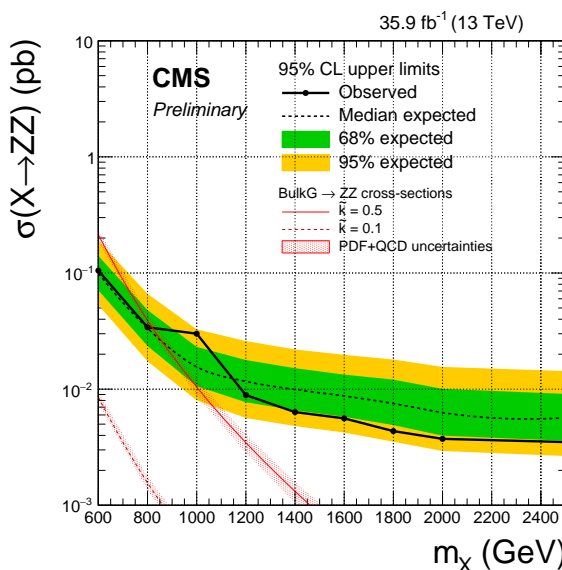


Figure 2.14: The observed and expected limits, with 68% and 95% uncertainty bands, on the product of the cross section and branching fraction $\sigma\mathcal{B}(G \rightarrow ZZ)$ for a spin-2 bulk graviton, as a function of the reconstructed mass of the diboson resonance. The colored lines show the theoretical predictions for $\tilde{k} = 0.1$ and 0.5 .

435 Similarly for ATLAS experiment, searches for diboson resonances in sec. 2.2.6 have been

2.3 Warped extra dimension

⁴³⁶ interpreted in the graviton context. The most stringent limit is given by [25], where, under the
⁴³⁷ assumption $\tilde{k} = 1$, a spin-2 bulk graviton with mass lower than 1.76 TeV is excluded (fig. 2.15).

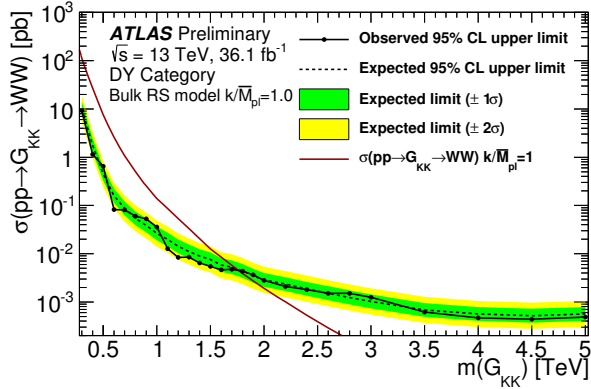


Figure 2.15: The observed and expected limits, with 68% and 95% uncertainty bands, on the product of the cross section and branching fraction $\sigma\mathcal{B}(G \rightarrow ZZ)$ for a spin-2 bulk graviton, as a function of the reconstructed mass of the diboson resonance. The colored lines show the theoretical predictions for $\tilde{k} = 1$.

The Large Hadron Collider and the CMS experiment

439

440

441 Brief intro to CERN and LHC

442 • research

443 • technology

444 • education

445 • collaboration

446

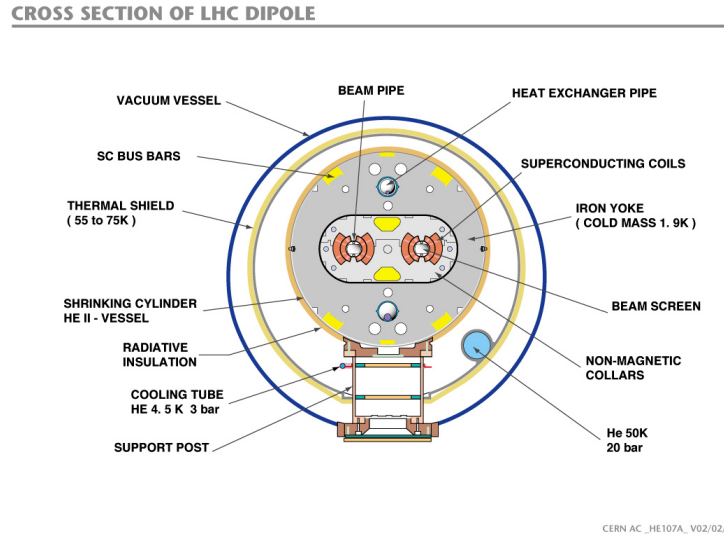
3.1 The Large Hadron Collider

447 The Large Hadron Collider (LHC) is a 27 km ring structure designed for the acceleartion
 448 and collision of protons and heavy ions. It is situated approximatively 100 m underground,
 449 between France and Switzerland, in the Geneva area, and it is the most important of the
 450 CERN (Conseil européen pour la recherche nucléaire) facilities. In order to reduce the cost of
 451 the project, definitively approved in 1996, the LHC has been designed to fit the pre-existing
 452 underground tunnel of the Large Electron-Positron collider (LEP) [ref. 24 Jacopo], built to
 453 accelerate electrons and positrons and running until the year 2000.

454 Moving from an electron-positron collider to an hadron collider allowed to reach higher ener-
 455 gies in the center-of-mass frame, since the synrocotron radiation loss is inversely proportional
 456 to the fourth power of the mass of the particle involved: hence, it is reduced by a factor
 457 $m_p/m_e \sim 10^3$. Furthermore, at a proton-proton collider it is possible to collect higher lumi-
 458 nosities (and hence more statistics) with regards to, for example, a proton-antiproton collider,
 459 like Tevatron at Fermilab, in the USA.

460 In the LHC two identical beam pipes rings are designed to let protons circulate in opposite
 461 directions, in ultrahigh vacuum conditions (10^{-11} - 10^{-10} mbar) in order to avoid collisions
 462 with gas molecules. Given the reduced available diameter in the tunnel (4 m), the two proton
 463 beams are magnetically coupled. The collider is composed by 8 arc sections (48 km) driving

464 protons around the ring, and straight sections (6 km) where beam control systems and detec-
 465 tors are inserted. Proton beams collide in four interaction points, where the four main LHC
 466 experiments are installed: ALICE, ATLAS, CMS, LHCb.



CERN AC _HE107A_ V02/02/98

Figure 3.1: Section of the LHC dipole magnet structure.

467 In fig. 3.1, a slice of the arc section is displayed. Around the beam pipes, two superconducting
 468 magnetic dipoles are located: they generate vertical magnetic fields in opposite directions.
 469 The superconducting coils are made of niobium-titanium, materials that are superconducting
 470 at very low temperature. At the LHC, they are kept at a temperature of 1.9 K (-271.3°C)
 471 by a closed liquid helium circuit. A current of 11850 A flows through the magnets, without
 472 any energy loss due to electrical resistance, generating a magnetic field of 8.33 T. Magnets
 473 of higher order in multipole expansion (quadrupoles, sextupoles, octupoles, ...) are used to
 474 optimize the proton trajectories; in particular, quadrupoles allow to focus and squeeze the
 475 beams. Along the LHC ring here are 9593 magnets; 1232 are dipoles, 392 are quadrupoles.
 476 The LHC represents the final step of the CERN accelerator complex, showed in fig. 3.2. Protons
 477 are extracted from hydrogen atoms and inserted in the linear accelerator Linac2, that brings
 478 them to an energy of 50 MeV. They circulate around a little synchrotron, Proton Synchrotron
 479 Booster, reaching an energy of 1.4 GeV, and then in the Proton Syncrhrotron (PS), where their
 480 energy is increased to 25 GeV. The second to last step is the Super Proton Synchrtotron, SPS,
 481 accelerating protons up to 450 GeV. They are finally injected in the Large Hadron Collider,
 482 where sixteen radiofrequency cavities (RF) accelerate protons inside each beam up to an en-
 483 ergy of 6.5 TeV, providing a center-of-mass energy of 13 TeV when colliding. The RF cavities
 484 provide an accelerating electromagnetic field up to 5 MV/m (maximum voltage of 2 MV),
 485 that oscillates with a frequency of 400 MHz. Like the magnets, the cavities are kept at low
 486 temperature (4.5 K, or -268.7°C) in order to allow superconducting conditions. The maximum
 487 beam energy can be reached in 15 minutes. After several hours of collisions (~ 10 hours), the
 488 quality of the beams deteriorates and they are extracted from the machine and dumped.
 489
 490 Protons circulate inside the LHC ring in bunches of $\sim 10^{11}$ particles each, 80 mm long. Fo-
 491 cusing magnets allow to reduce the bunch diameter down to 16 μm . Different bunches are
 492 separated by 25 ns (or, ~ 7.5 m), corresponding to a frequency of 40 MHz and an instant-

3.1 The Large Hadron Collider

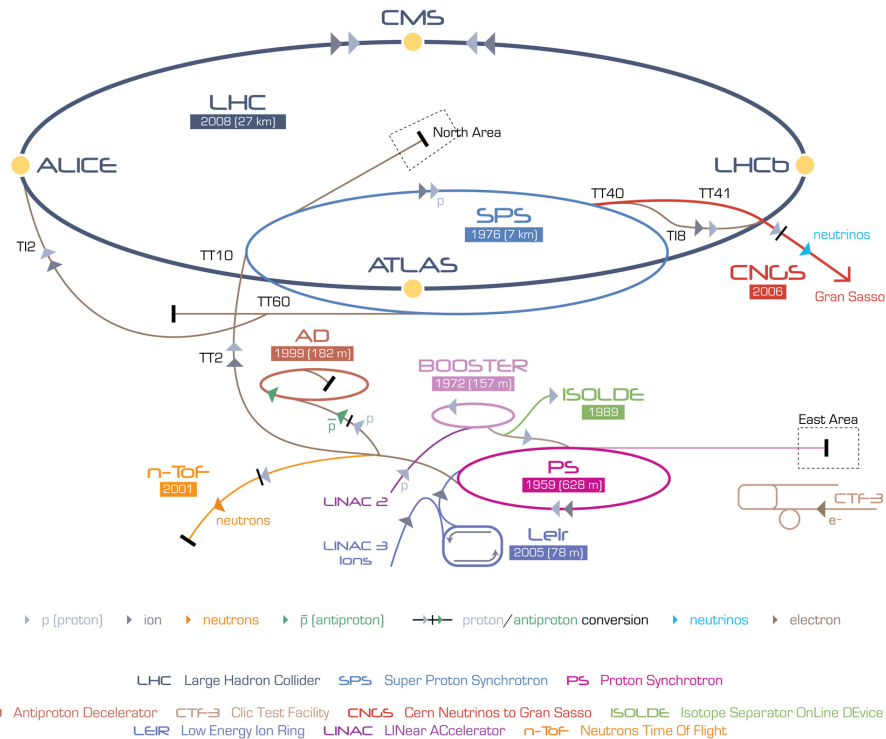


Figure 3.2: The CERN accelerator complex.

neous (peak) luminosity (defined in eq. 3.1) of $1.2 \times 10^{34} \text{ cm}^{-2}\text{s}^{-1}$. Given the structure of the beams, at every bunch crossing many protons interact simultaneously: this phenomenon is called pile-up. The designed maximum number of bunches is 2808.

The main parameters that describes an hadronic collider are the center-of-mass energy, corresponding to the sum of the energies of the beams, and the instantaneous luminosity, that describes the frequency of the interactions among the bunches in the beams. If the bunches in the first beam contain n_1 protons, and the bunches in the second beam contain n_2 protons, and if the colliding area is Σ , the frequency of complete turns around the ring is f , the instantaneous luminosity $\mathcal{L}_{\text{inst}}$ is:

$$\mathcal{L}_{\text{inst}} = f \frac{n_1 n_2}{\Sigma}. \quad (3.1)$$

If a generic physics process i has a cross-section of σ_i , the interaction rate R_i is:

$$R_i = \frac{dN_i}{dt} = \sigma_i \mathcal{L}_{\text{inst}}, \quad (3.2)$$

and the number of events recorded in the time interval $(0, \tau)$ is obtained by the integrated luminosity $\mathcal{L} = \int_0^\tau \mathcal{L}_{\text{inst}} dt$:

$$N_i = \sigma_i \int_0^\tau \mathcal{L}_{\text{inst}} dt. \quad (3.3)$$

In fig. 3.3, a summary of the luminosity measurement in 2016 data is presented. The luminosity delivered by LHC is represented in blue, the recorded by CMS is in orange. The mean number of interaction per bunch crossing (pile-up) is presented as well. The average number of interactions per collision is 27, the maximum is around 50.

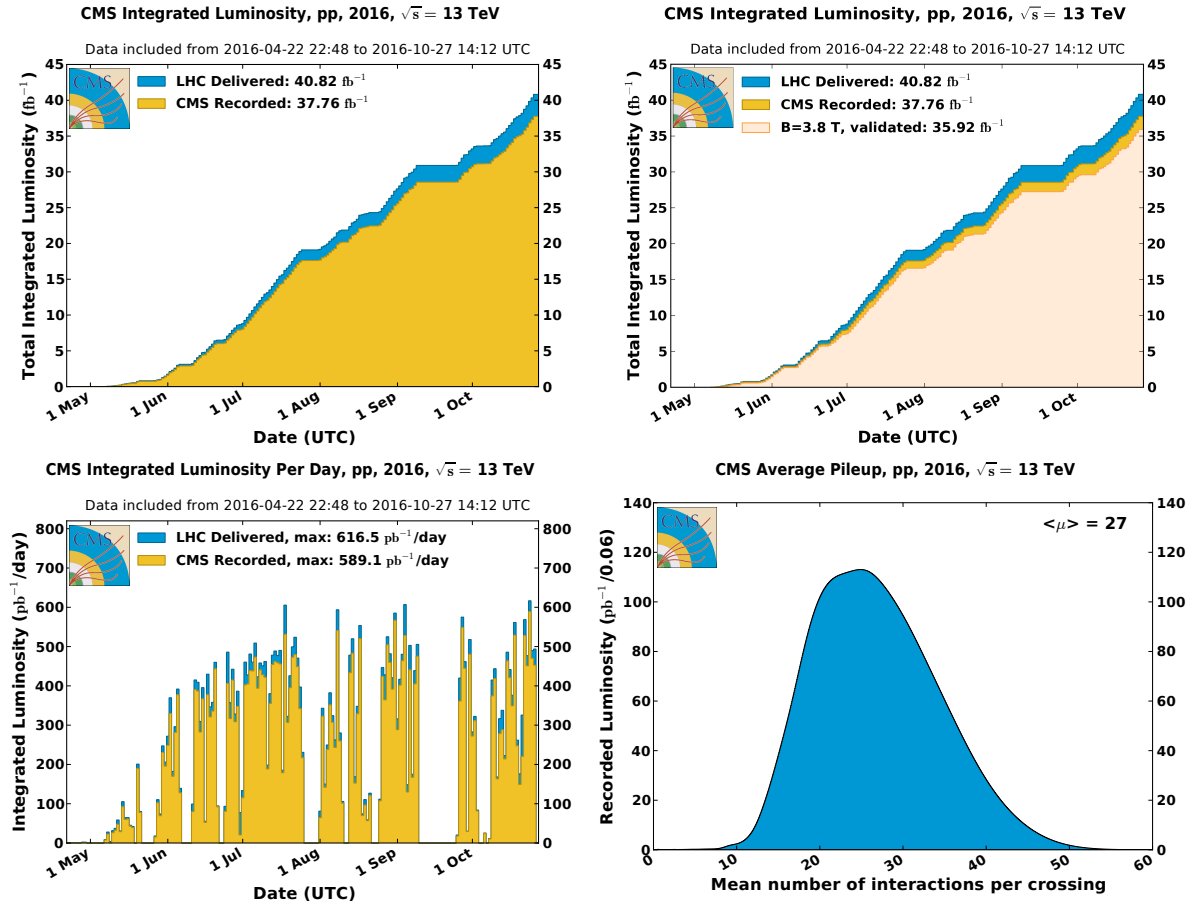


Figure 3.3: Luminosity in 2016 LHC data. Top-left plot: the cumulative integrated luminosity delivered by LHC (in blue) and recorded by CMS (in orange), as a function of the data taken period. Top-right plot: data recorded by CMS and declared as optimal for the physics analyses (in light orange), corresponding to a total integrated luminosity of 35.9 fb^{-1} . Bottom-left plot: maximum integrated luminosity per day. Bottom-right plot: number of proton interactions per bunch crossing (pile-up).

510 3.1.1 Proton-proton interactions

- 511 Proton-proton collisions allow to reach higher energies and luminosities, but the drawback is
 512 the complexity of the events when compared to electron-positron collisions: not only because
 513 of the increasing backgrounds due to strong interactions among partons, but also because the
 514 momenta of the proton partons taking part in the interaction are unknown; not to mention the
 515 problem of disentangling the tracks of the particles coming from the interesting hard interac-
 516 tions from the spectator pile-up interactions (in fig. 3.4, 78 proton collisions were happening
 517 at the same bunch crossing).
 518 The majority of the LHC events is represented by soft interactions, with low transverse mo-
 519 mentum transfer, namely elastic and diffractive scatterings. In the so-called hard interactions,
 520 on the other hand, the transferred momentum among particles is high, allowing to produce
 521 massive resonant phenomena. These events manifest in peculiar final state signatures that can
 522 be distinguished from the soft interaction background.

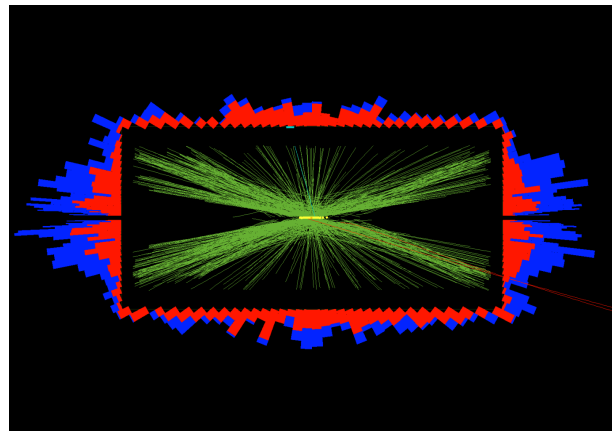


Figure 3.4: 78 events.

523 At high momentum transfer (perturbative regime), a proton can be described as a collection
 524 of partons, each bringing a fraction x of the initial beam momentum, whose distribution is
 525 described by the parton distribution functions (PDF), $f(x, Q^2)$, as a function of the Bjorken's
 526 variable and of the momentum transfer Q^2 . At very high center-of-mass energies (13 TeV), the
 527 proton masses can be neglected; the available energy in the parton 1 and parton 2 scattering
 528 is unknown, $\sqrt{x_1 x_2 s}$. The total cross-section is given by:

$$\sigma = \int dx_1 f_1(x_1, Q^2) \int dx_2 f_2(x_2, Q^2) \sigma_{12}(x_1 p_1, x_2 p_2, Q^2), \quad (3.4)$$

529 where σ_{12} is the cross-section at parton level, and f_1, f_2 are the parton PDFs. In fig. 3.5, parton
 530 cross-sections are displayed as a function of the center-of-mass energy.

531 3.2 CMS detector

532 The Compact Muon Solenoid (CMS) is a multi-purpose detector built in the LHC ring. It is
 533 situated in a cavern 100 m underground, near Cessy, in France. It is a cylinder 22 m long, with
 534 a diameter of 15 m, and a weight of 12500 tons. Its physics programme includes the search
 535 for the Higgs boson (discovered in 2012), precision measurements of the Standard Model pa-
 536 rameters and rare decays (physics of beauty quark), and search for new physics beyond the
 537 standard model (SUSY, exotic phenomena, dark matter, extra dimensions).

538 The CMS detector is structured in many layers of sub-detectors, giving different responses
 539 depending on the nature and the momentum of the particle passing through. The inner de-
 540 tectors have been finely segmented in order to afford the high radiation levels and particle
 541 multiplicity at the interaction point, so that the reduced occupancy of each layer allows to
 542 measure and distinguish precisely the primary vertices of the hard interactions from the pile-
 543 up events. A very precise time resolution is vital in order to synchronize all the subsystems
 544 together.

545
 546 Fig. 3.6 shows a sketch of the CMS detector. It is longitudinally segmented in the barrel region
 547 and two endcaps. In the forward region (over the endcaps), where the beam radiation is very
 548 intense, additional calorimeters have been placed. In fig. 3.7, the mean path of a specific
 549 particle through the sub-detectors is represented, depending on its flavour.

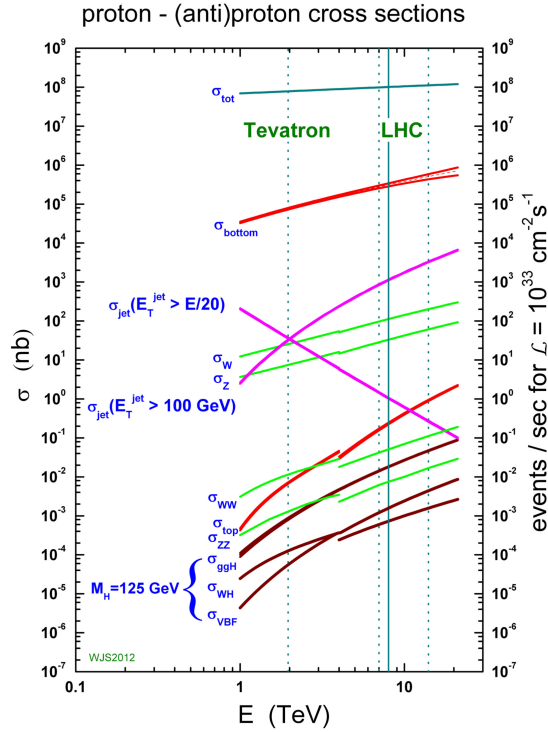


Figure 3.5: Cross-sections and number of expected events in proton-proton collisions, as a function of the center-of-mass energy. Rare phenomena, such as the Higgs boson production, can be observed at the LHC.

550 3.2.1 The coordinate system

551 The CMS coordinate system is depicted in fig. 3.8. x and y are the coordinates in the transverse
 552 plane, z is the longitudinal coordinate. The x axis points at the center of the LHC ring, the y
 553 axis points upward, the z axis is along the beam direction. The azimuthal angle ϕ lays in the
 554 in the transverse plane, and it is measured starting from the x axis; the radial coordinate is r .
 555 The polar angle θ lays in the plane rz . The transverse component of the 3-momentum, \vec{p}_T , is
 556 orthogonal to the beam axis and lays in the plane xy . The transverse energy is defined as the
 557 magnitude of \vec{p}_T : $E_T = E \sin \theta$.

558 Two other commonly used variables are the rapidity, y , and pseudorapidity, η , defined as
 559 functions of the particle energy E , the longitudinal component of the momentum p_z and the
 560 3-momentum modulus:

$$y = \frac{1}{2} \log \frac{E + p_z}{E - p_z} \quad (3.5)$$

$$\eta = \frac{1}{2} \log \frac{|\vec{p}| + p_z}{|\vec{p}| - p_z} = -\log \tan \frac{\theta}{2}.$$

561 When the considered particle is produced in the forward region, hence at $\theta = 0$, $\eta \rightarrow \infty$. When
 562 the particle is produced in the transverse plane, hence $\theta = \pi/2$, $\eta = 0$. At high energies, when
 563 the masses can be neglected, rapidity and pseudorapidity coincide; these variables are largely
 564 used at colliders because they are invariant under Lorentz boosts along the beam direction.

CMS Detector

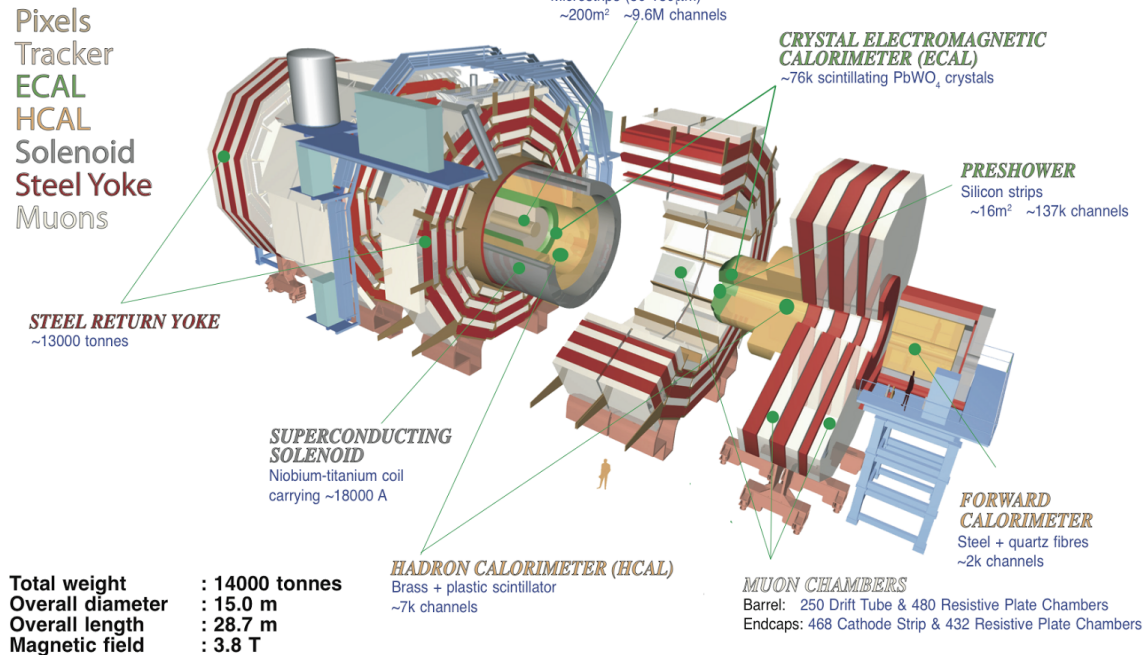


Figure 3.6: The CMS experiment.

565 3.2.2 The magnet

566 The CMS superconducting magnet is an hollow cylinder (13 m long, 6 m of diameter, showed
 567 in fig. 3.9). In the niobium and titanium fibers that constitute the solenoid, an electrical
 568 current of 19 kA flows, providing a maximum magnetic field of 3.8 T and storing a maximum
 569 energy of 2.6 GJ. Superconducting conditions are allowed by a liquid helium cooling system,
 570 keeping the solenoid at 4.5 K. In order to avoid stray fields, the magnetic field lines are closed
 571 by the return yoke, composed by 10 ktons of magnetized iron blocks, located in the outer
 572 part of CMS and alternated to the muon chambers. The homogeneous magnetic field inside
 573 the detector bends the trajectories of the charged particles, allowing the measurement of their
 574 momenta p , given the relation with the magnetic field strength B and the radial coordinate R
 575 of the trajectory:

$$p[\text{GeV}] = 0.3 \times B[\text{T}] \times R[\text{m}]. \quad (3.6)$$

576 3.2.3 The tracking system

577 The CMS tracking system is composed by a cylinder of silicon detectors (2.5 m of diameter
 578 and 5.8 m length). Their design allows a precise reconstruction of the tracks left by charged
 579 particles and of the interaction vertices, a fundamental tool to identify heavy quarks (charm,
 580 beauty) and leptons (taus). Tracker detectors cover a pseudorapidity region of $|\eta| < 2.5$ and
 581 have an active area of 210 m^2 . The two sub-detectors of the tracking system are the pixel

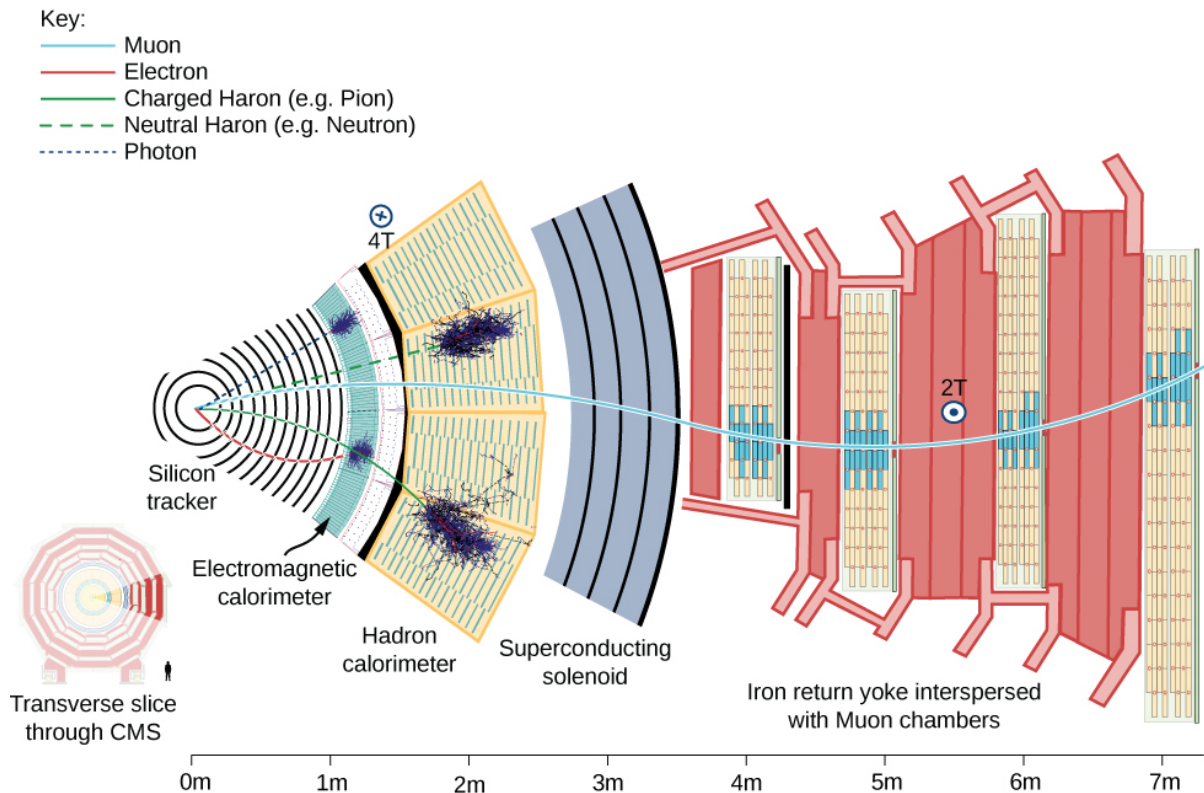


Figure 3.7: Mean path of a particle through the CMS detector. A muon, in light blue, passes through with a bended trajectory, depending on its momentum and charge, triggering signals in all the sub-systems. An electron, in red, leaves a track in the silicon tracker and is absorbed by the electromagnetic calorimeter. A neutral or charged hadron, in green, stops inside the hadronic calorimeter. A photon, dotted blue line, showers in the electromagnetic calorimeter, without leaving any track in the silicon detector.

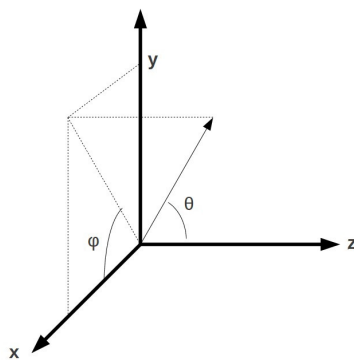


Figure 3.8: CMS coordinate system.

detector, closer to the interaction point, and the strip detector, covering a radius of 0.2 – 1.2 m. The high granularity of the pixels and micro strips allows to keep the occupancy at acceptable levels, given the high multiplicity of the tracks ($\sim 1 \text{ MHz/mm}^2$). The silicon detectors and the electronic cables are cooled down to a temperature of $\sim 10^\circ \text{ C}$. The structure of the tracking

3.2 CMS detector

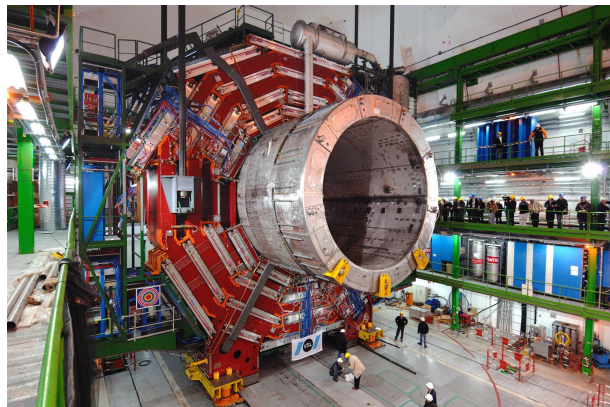


Figure 3.9: Installation of the superconducting solenoid in the CMS cavern.

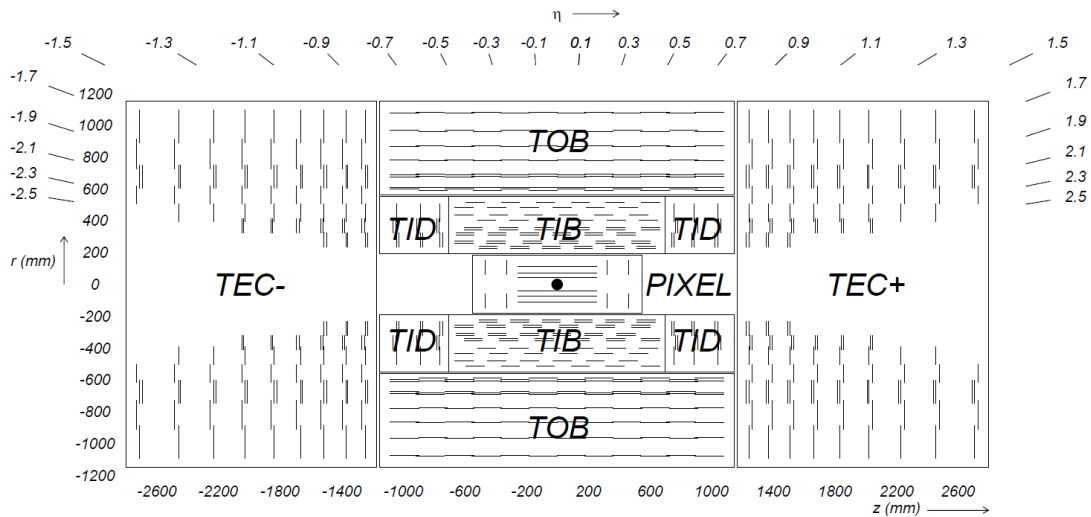


Figure 3.10: The CMS tracking system: the inner pixel detector, close to the interaction point, and the outer strip detector.

586 system is showed in fig. 3.10.

587 **3.2.3.1 The pixel detector**

588 The pixel detector is composed by 66 millions of silicon cells, whose dimensions are $100 \times$
 589 $150 \mu\text{m}^2$, $285 \mu\text{m}$ of thickness, placed in 1440 modules. Silicon cells are set in three layers in
 590 the barrel region and in two disks at each endcap. Barrel modules are disposed parallel to
 591 the magnetic field, whilst at the endcap they are tilted by about 20° . Pixels allow a spatial
 592 resolution of $10 \mu\text{m}$ in the transverse plane, and of $\sim 20 \mu\text{m}$ along the longitudinal coordinate.
 593 Their reduced size guarantees an occupancy of 10^{-4} per pixel at each bunch crossing, in high
 594 luminosity regime.

595 **3.2.3.2 The strip detector**

596 The strip system is divided in the four-layered tracker inner barrel (TIB), covering a region
 597 $20 < r < 55 \text{ cm}$ with respect to the interaction point, the six-layered tracker outer barrel (TOB),

598 located at $55 < r < 110$ cm, the three tracker inner disks (TID) and the nine tracker endcaps
 599 (TEC) at each cylinder base. Given the lower radiation level at higher radii (and hence a lower
 600 occupancy, around few percent), micro strips are bigger than the pixels. Silicon strips in TIB
 601 and TID are $320\ \mu\text{m}$ thick, 10 cm long, and with a pitch ranging from 80 to $120\ \mu\text{m}$; strips in
 602 TOB and TEC are 25 cm long, with a different thickness ($320\ \mu\text{m}$ for TID, $500\ \mu\text{m}$ for TEC)
 603 and pitch (97–184 μm). There are 15148 strip modules, and 9.3 million readout channels. The
 604 strip spatial resolution is about $20 - 50\ \mu\text{m}$ in the transverse plane and about $200 - 500\ \mu\text{m}$
 605 along the longitudinal coordinate.

606 3.2.4 The electromagnetic calorimeter

607 The CMS electromagnetic calorimeter (ECAL, shown in fig. 3.11) is a homogeneous detector
 608 composed by lead tungstate (PbWO_4) scintillating crystals, designed to measure the energy
 609 deposits of photons and electrons through their electromagnetic showers. PbWO_4 is transpar-
 610 ent and dense ($8.3\ \text{gr}/\text{cm}^3$); it has a fast time response (the 85% of the scintillating light is
 611 emitted at every bunch crossing, namely 24 ns), high scintillating efficiency and radiation re-
 612 sistance; it has a radiation length is $X_0 = 0.89\ \text{cm}$ and a Molière radius of $2.19\ \text{cm}$. The ECAL is
 613 divided in the barrel region ($\eta < 1.479$, at a radius of 1.3 m) and the endcaps ($1.479 < \eta < 3$).
 614 The 61200 crystals employed in the barrel region, whose size is $(22 \times 22)\ \text{mm}^2 \times 23\ \text{cm}$, have
 615 a radiation length of $25.8X_0$; the 7324 crystals in the endcaps, $28.6 \times 28.6\ \text{mm}^2 \times 22\ \text{cm}$, have
 616 a radiation length of $24.7X_0$. Before the endcaps, on each side, a pre-shower detector is in-
 617 stalled: it is composed by two disks of lead absorber and two layers of silicon strips, up to a
 618 radiation length of $3X_0$. It has been designed to distinguish the photons coming from the π^0
 619 decay from the rare Higgs decay $H \rightarrow \gamma\gamma$. The readout and amplification of the scintillating
 620 light, performed by avalanche photodiodes in the barrel and by vacuum phototriodes in the
 621 endcaps, requires a stable temperature of $18^\circ\ \text{C}$, mantained by a water cooling system.

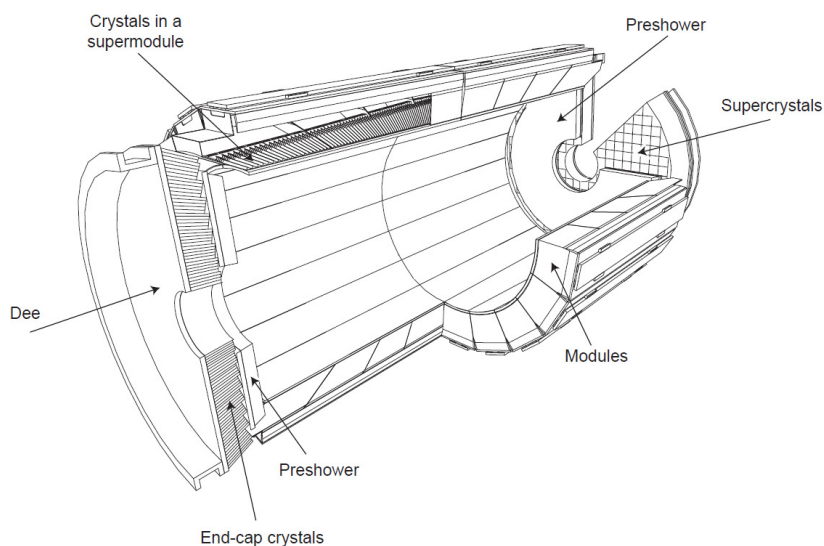


Figure 3.11: The CMS electromagnetic calorimeter.

3.2 CMS detector

622 Controlla nuove calibrazioni The energy resolution of the calorimeter is parametrized as:

$$\left(\frac{\sigma}{E}\right)^2 = \left(\frac{S}{\sqrt{E}}\right)^2 + \left(\frac{N}{E}\right)^2 + C^2, \quad (3.7)$$

623 where $S = 0.028 \text{ GeV}^{\frac{1}{2}}$ is the stochastic term, $N = 0.12 \text{ GeV}$ is related to noise contribution,
624 and $C = 0.003$ is a constant term depending on the calibration.

625 3.2.5 The hadronic calorimeter

626 The hadronic calorimeter (HCAL, displayed in fig. 3.12) is a sampling calorimeter, composed
627 by brass and plastic scintillator layers. It has been designed in order to guarantee a good
628 hermeticity, allowing to perform a precise measurement of the missing transverse energy. It is
629 located within the electromagnetic calorimeter and the solenoid, covering a region of $|\eta| < 1.3$
630 in the barrel, and $1.3 < |\eta| < 3$ in the endcaps. Brass is non-magnetic and has short interac-
631 tion length (16.4 cm): the 60 mm thick absorber layers used in the barrel allow to reach 5.6
632 interaction lengths at $\eta = 0$ and 10.8 interaction lenghts at $\eta = 1.3$; the 80 mm thick layers in
633 the endcaps reach 11 interaction lenghts. An additional calorimetric layer has been installed
634 out of the solenoid, in order to reach 11.8 interaction lenghts in the barrel region. The scin-
635 tillation light, typically in the blue-violet region of the electromagnetic spectrum, is collected
636 by wavelenght-shifter fibers, translated and amplified by multi-channel hybrid photodiodes,
637 proportionally to the magnitude of the energy deposits. An additional hadronic calorimeter
638 has been placed in the forward region, $3 < |\eta| < 5.2$, at 11.2 m from the interaction point.
639 It has beeen designed to afford the high levels of radiations: it is composed by 55 mm thick
640 absorber layers of stainless-steel, and quartz fibers, able to detect the Cherenkov scintillating
641 light of the charged particles of the hadronic showering. A longitudinally segmentation allow
642 to distinguish hadronic particles from electromagnetic components. The energy resolution of
643 the hadronic calorimeter is:

$$\left(\frac{\sigma}{E}\right) \approx \frac{a}{\sqrt{E}} \oplus b\%, \quad (3.8)$$

644 where $a = 65\%$ in the barrel region, 85% in the endcaps, 100% in the forward region, and
645 $b = 5\%$.

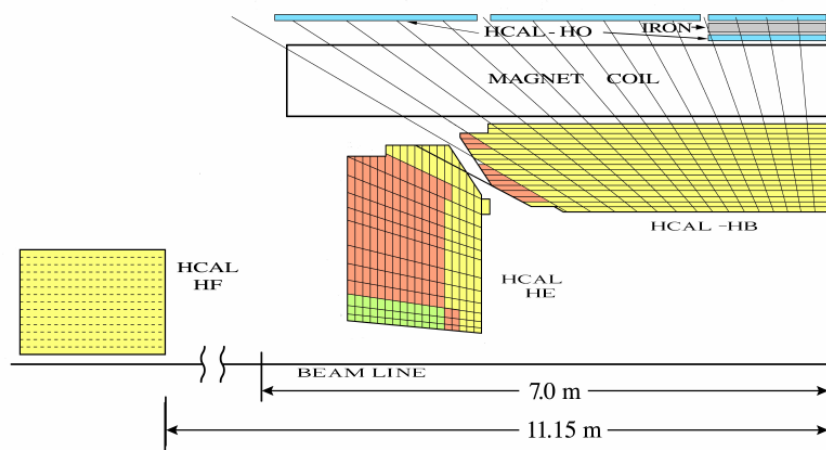


Figure 3.12: The CMS hadronic calorimeter.

3.2.6 The muon system

The outer system of the CMS experiment consists into gas detectors for identifying muons, that are located between the iron return yokes, designed to close the magnetic field generated by the solenoid. In the barrel region, where a smaller number of muons is expected and the magnetic field is less strong, Drift Tubes (DT) detectors are installed. In the endcaps, where the flux of particles is larger, Cathod Strip Chambers (CSC) are used, and disposed in three disks. CSCs are designed to allow faster responses, higher granulatiy and radiation resistance. Resistive Plate Chambers (RPC) are installed both in the barrel and in the endcaps as additional triggering system. The geometry of the muon system is showed in fig. 3.13; it consists of 250 DTs, 530 CSCs, 610 RPCs, and it covers a region $|\eta| < 2.4$.

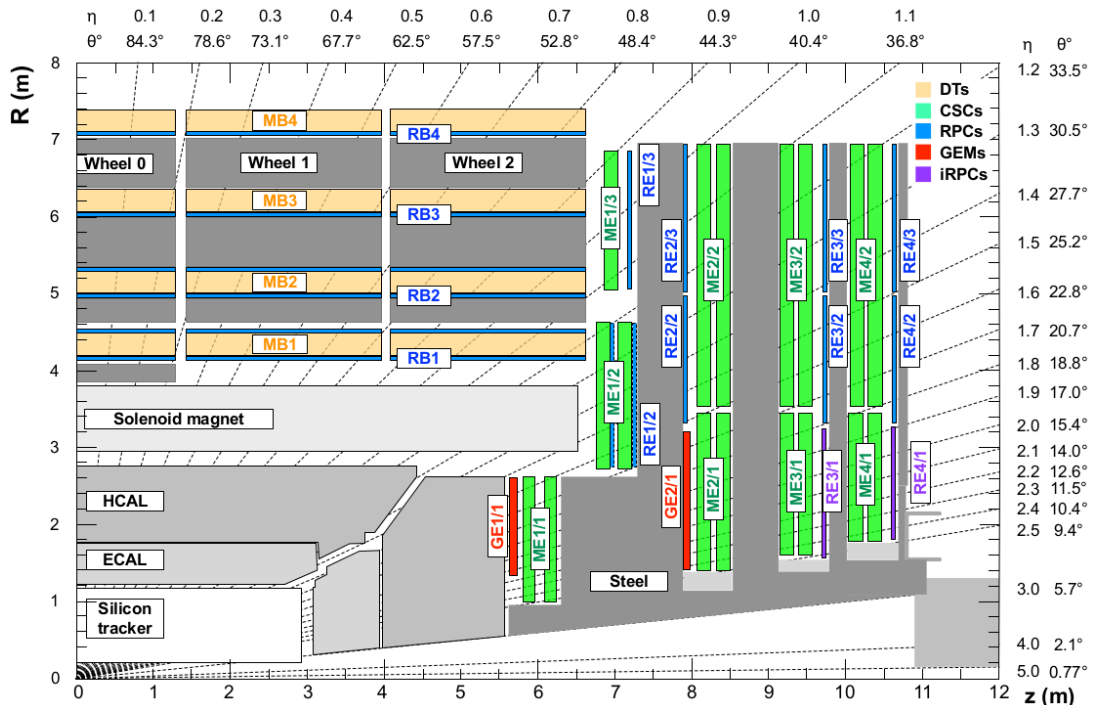


Figure 3.13: Section of CMS detector, in the plane $r z$, parallel to the beamline, that emphasizes the location of the muon detectors, in particular: Drift Tubes (DT, in yellow); Cathode Strip Chambers (CSC, in green); Resistive Plate Chambers (RPC, in blue).

3.2.6.1 The Drift Tubes

Drift Tube detectors cover a region of $|\eta| < 1.2$ and are arranged in four stations, segmented along the beam line in five wheels. The basic element of the detector is the cell, that has a size $42 \times 13 \text{ mm}^2$. Each cell is filled with a gas mixture (85% argon, 15% CO_2), in which the process of ionization takes places; the ionization electrons drift from the $50 \mu\text{m}$ thick steel anodic wire, in the center of the cell, towards the aluminium cathodic strips, located at its edge. Additional electrodes on the surface of the cells allows to shape the electric field, in order to make the drift speed of the electrons uniform: the muon position is then extrapolated from the measurement of the drift time. Every station is composed by three cells superlayers. In the inner and the outer superlayers, the cells are oriented such in a way that the anodic

3.2 CMS detector

666 wire is located along the z axis, in order to measure the ϕ coordinate. In the intermediate
667 superlayer, wires are parallel to the radial coordinate, hence they can measure the z position.
668 The spatial resolution of the system is $100\ \mu\text{m}$ in the $r\phi$ plane, 1 mrad in the ϕ coordinate, and
669 $150\ \mu\text{m}$ in the longitudinal z coordinate.

670 **3.2.6.2 The Cathode Strip Chambers**

671 Cathode Strip Chambers cover a region of $0.9 < |\eta| < 2.4$, overlapping with the DT in the
672 pseudorapidity range $0.9 < |\eta| < 1.2$. The anodic wires inside each CSC are located into six
673 planes, with the aim of measuring the radial coordinate; the wire planes are perpendicularly
674 crossed by cathodic strips, disposed along the radial direction to measure the ϕ coordinate.
675 Ionization electrons produced by muons passing through the gas mixture in the chambers
676 migrate towards the anode, inducing a charge distribution on the cathodes, from which the
677 azimuthal coordinate can be reconstructed. The spatial resolution in the r coordinate is $200\ \mu\text{m}$,
678 and it is $75 - 150\ \mu\text{m}$ in the $r\phi$ plane. CSCs are arranged in four disks and in three
679 concentric rings.

680 **3.2.6.3 The Resistive Plate Chambers**

681 Resistive Plate Chambers (RPC) are located both in the barrel (disposed in six layers) and in
682 the endcap region (three layers), up to a pseudorapidity of $|\eta| < 1.6$. These gas detectors
683 are charged at very high voltages, in order to work in the avalanche ionization mode. The
684 plastic resistive plates are equipped with readout strips. The spatial resolution of the detector
685 is low (1-2 cm), but the fast timing response (2-3 ns) and good time resolution (1 ns) allow to
686 employ RPCs as an additional triggering system and to profit of a precise measurement of the
687 bunch-crossing time.

688 **3.2.7 The trigger system and data acquisition**

689 The CMS trigger system has been designed considering the high instantaneous luminosity,
690 such that it can provide a fast response and it allows to reduce the nominal event rate of
691 40 MHz in proton proton collision. The complexity of the CMS detector and the very high
692 number of readout channels result into a huge amount of data per event, approaching the
693 order of few MB per bunch crossing, hence 40 TB per second. The handling and the recording
694 of data is currently limited at the order of ~ 100 Hz; hence, applying online selections to
695 skim the events that are going to be written on tape, without rejecting interesting signals of
696 hard processes and rare phenomena becomes a crucial and challenging point for every data
697 analysis. Events are filtered by trigger selections at different levels: the Level-1 (L1) trigger
698 is an hardware device, that allows to reduce the event rate from 40 MHz to the order of 100
699 kHz; the High Level Trigger (HLT) is a set of software algorithms that skims the event rate
700 down to few hundred Hz. Once the trigger decisions are taken, the final events are handled
701 by the Data Acquisition System (DAQ), that collects the informations coming from to the
702 subdetectors and sends them to the storage devices.

703 **3.2.7.1 The Level-1 trigger**

704 The L1 trigger is an hardware device composed by customized electronics, and it accesses
705 the informations coming from the calorimeters and the muon system, while the tracker is not

706 considered given the excessively large bandwidth needed by its readout channels. The L1
 707 trigger perform a first raw local reconstruction of each object, called “trigger primitive”. The
 708 L1 trigger is composed by three subsystems: the calorimeter trigger, the muon trigger (divided
 709 in three independent sub-subsystems for each muon subdetector, namely DTs, RPCs and
 710 CSCs), and the global trigger, that combines the informations of the former subsystems. The
 711 best quality trigger primitives reconstructed by the calorimeter and muon detectors (namely,
 712 roughly reconstructed electrons, photons, muons, jets, jets coming from the hadronic decays
 713 of tau leptons, and missing energy) are handled by the global trigger, who takes the decision
 714 of discarding or keeping the event every 3.2 μ s. The simplest trigger selections require the
 715 presence of a single object, whose energy or transverse momentum is higher than a certain
 716 threshold; more complicated triggers involve multiple objects or geometrical selections, that
 717 can be performed in parallel up to 128 simultaneous requirements.

718 **3.2.7.2 The High Level Trigger**

719 The HLT skims the L1 output rate down to few hundreds of Hz by applying a set of algo-
 720 rithms implemented in the same software used for the offline analysis, consisting in the event
 721 reconstructions exploiting the whole informations coming from all subdetectors. The comput-
 722 ing time is still a crucial factor, hence selections applied to HLT physics objects are generally
 723 less accurate than those of the offline analysis; furthermore, HLT can discard the event even
 724 before its full reconstruction (*i.e.* by looking only at certain region of the detectors). Events
 725 filtered by the HLT decisions are assigned to precise trigger paths and recorded in precise
 726 categories of datasets.

727 **3.2.7.3 Data acquisition, computing and storage**

728 The DAQ system deals with the storage, transfer and handling of the data collected by CMS;
 729 it also supports and stores the data simulations and calibrations of the subdetectors. The
 730 CMS computational resources are located in worldwide distributed data nodes, called Tiers.
 731 The CMS software (CMSSW) is based on an object oriented architecture (mainly C++). The
 732 basic unity of every data, both real and simulated ones, is the Event, that could contain very
 733 rough informations (RAW data format) or higher level refined objects (AOD, Analysis Object
 734 Data) where all the calibrations and corrections needed to properly deal with the final physics
 735 objects are already in place. Data are handled by C++ or python modules, and the outputs
 736 are written in ROOT files. [cittazione]

737 **3.2.8 Particle Flow event reconstruction**

738 The particle flow (PF) algorithm [ref. paper] aims at identifying and reconstructing each par-
 739 ticle produced by the proton-proton collisions, combining the informations coming from all
 740 the CMS subdetectors. It is particularly suitable to improve the reconstruction of jets, missing
 741 transverse momentum (used to identify neutrinos) and hadronically decaying tau leptons.
 742 The association of the informations is performed at different stages. The reconstruction of
 743 the charged particles in the silicon detector is performed with an iterative algorithm, and the
 744 reconstructed object is called a tracker track. Then, a clustering algorithm is performed to col-
 745 lect and combine the energy deposits in the calorimeters, in such a way to distinguish neutral
 746 from charged particles, reconstruct their directions, improve the energy measurement of the

3.2 CMS detector

747 very energetic charged particles, whose tracks are less bended by the magnet and hence less
748 precisely determined. The last informations are provided by the hits collected in the muon
749 system. The three sets of reconstructions are then combined with a link algorithm, that aims
750 at associating tracker tracks to calorimeter clusters and muon hits with geometrical criteria. A
751 track in the silicon detector is linked to a calorimeter cluster if the extrapolated position lies
752 in the cluster itself. Similarly, clusters in different calorimeters are linked when the position
753 in the more granular calorimeter (*i.e.* ECAL) lies in the envelope of the clusters in the less
754 granular calorimeter (*i.e.* HCAL). The decision of linking a tracker track to a muon track is
755 based on the χ^2 of a global fit between the two tracks.

756 The particle flow algorithm then interprets the collected and linked informations as different
757 particles. Muons are identified by the combination of a track in the silicon detectors and a
758 track in the muon chambers. Photons are determined directly by ECAL clusters. Electrons
759 energies and positions are measured by ECAL clusters, linked to a corresponding tracker
760 track, and considering all the energy clusters produced by the bremsstrahlung photons radi-
761 ated while interacting with the material. The hadrons are identified by the tracks (if charged)
762 linked to the corresponding ECAL and HCAL clusters. The hadron energy resolution, 10%
763 at 100 GeV combining ECAL and HCAL, is such that neutral hadrons can be distinguished
764 as an energy calorimetric excess when overlapped by a charged hadron occupying the same
765 calorimetric towers. Finally, the missing transverse momentum is defined as the negative sum
766 of the transverse momenta of all the particles identified by the PF algorithm.

767

768 3.2.9 Physics objects

769 3.2.9.1 Track reconstruction

770 The reconstruction of the trajectories of the charged particles passing through the CMS de-
771 tector is performed by multiple iterations of the Combined Track Finder algorithm, that is
772 based on a Kalman filter approach [73 A]; given the high multiplicity of particles produced
773 at each bunch crossing and the multiple scatterings throughout the detector materials, this
774 represents a challenging task. The CTF algorithm builds a track starting from the so-called
775 seeds, namely triplets of hits collected in the pixel detector inner layers, or couples of hits
776 if the track originates from the interaction point. The initial guess of the track given by the
777 seeds is then extrapolated to the outer layers: if other hits are found to be compatible with
778 the trajectory hypothesis (χ^2 -based hypothesis test), they are added to the track. Once the outer
779 layers are reached, another reconstruction is performed backward, in order to clean the track
780 from spurious hits and enhance the tracking efficiency. The final collected hits are re-fitted
781 with Kalman Filter and more precise algorithms, in order to improve the quality of the mea-
782 surement. If two tracks share more than a half of their hits, the worst quality track is rejected.
783 The track reconstruction efficiency for particles with $p_T > 0.9$ GeV is 94% in the barrel and
784 85% of the endcap region [72 A].

785

786 3.2.9.2 Electrons and photons reconstruction

787 Electrons are reconstructed combining a track with the energy deposits clustered in the ECAL,
788 due to the showering of the electron through the detector and the emission of bremsstrahlung

photons. The combination can proceed both from the silicon detector in the outgoing direction and in the opposite way: the tracker seeding as starting point is suitable for low energy electrons, whose trajectories are less bended and hence more accurately measured by the tracker system; the grouping of ECAL clusters (called superclusters) followed by a consecutive track extrapolation, performed by taking into account the electron interaction with the detector material, is more efficient in case of high energetic electrons, due to the higher resolution of the ECAL scintillating crystals. A Gaussian-sum filter algorithm (GSF) [ref 78 alberto] allows to properly take into account the effects of the bremsstrahlung radiation, that is distributed not as a single Gaussian (standard Kalman filters) but rather as a sum of Gaussian functions.
 The identification of an electron relies on three groups of variables: observables combining measurement performed in the silicon detectors and in the calorimeter; purely calorimetric observables; purely tracking informations. Different selections are used for electron candidates found in the barrel and in the endcaps, and they can vary from loose criteria (high detection efficiency but less purity, namely more contamination from object misidentified as electrons) to tight criteria. Data and Monte Carlo simulations reproducing Z , ν and J/Ψ decays in e^+e^- are used to study the optimal working points, each one targeting at a different purity.
 The electron energy is determined correcting the raw energy measurement of the ECAL superclusters by taking into account the effects of the losses due to radiation or gaps between the calorimeter modules, and the pile-up contribution. The electron momentum resolution has been measured in $Z \rightarrow e^+e^-$ decays in Run 1 LHC data, and it varies from 1.7 to 4.5% depending on the pseudorapidity range. [arXiv 1502.02701] The electron isolation variable is defined as the p_T sum of the charged and neutral particles laying in a cone of $\Delta R = 0.3$ around the electron trajectory, divided by the transverse momentum of the electron:

$$I_{\Delta R=0.3}^e = \frac{\sum_{\text{char. hadrons}} p_T + \max \left[0, \sum_{\text{neut. hadrons}} p_T + \sum_{\text{photons}} p_T - 0.5 \sum_{\text{pile-up char. hadrons}} p_T \right]}{p_T^e}; \quad (3.9)$$

the contribution of the pile-up charged particles is removed. The isolation variable is used to distinguish electrons coming from the leptonic decays of electroweak bosons (low $I_{\Delta R=0.3}^e$) from electrons coming from the decays of heavy fermions, when they are more likely produced in association with light flavour jets and hence topologically close to calorimetric deposits due to hadrons (high $I_{\Delta R=0.3}^e$).

Photons are reconstructed with the ECAL clusters only. Given their importance in the discovery of the Higgs boson, dedicated studies have been performed both in data and in Monte Carlo simulations reproducing the $H \rightarrow \gamma\gamma$ process. Particular care has been taken in the treatment of the photon conversions into electron-positron pairs while interacting with the tracker detector. Dedicated selections allow to define different photon identification working points. Similarly to the case of the electrons, the photon isolation variable can be defined. The photon energy resolution varies from 1% to 3%, depending on the η range. [arXiv 1502.02702]

3.2.9.3 Muon reconstruction

A muon candidate can be built exploiting the hits collected in the silicon tracker (track) and in the muon system (standalone muon). Each muon subdetector (DTs, RPCs and CSCs) performs a local reconstruction of the candidate; the informations from the three muon chambers are combined with a Kalman filter approach.

3.2 CMS detector

Three different strategies are adopted to define a muon candidate in the CMS detector. A standalone muon is reconstructed by only using the local reconstruction in the muon chambers. A tracker muon is built starting from a track in the silicon detector, that is extrapolated up to the muon chambers, taking into account the multiple scattering and the energy loss through the material. The tracker muon is defined if at least one segment, *i.e.* a short track built with CSCs or DTs hits, is matched to the starting track. This technique is the most efficient for the reconstruction of low energetic muons. A global muon is built starting from a standalone muon, and then its trajectory is extrapolated towards the inner layer of the silicon detector and eventually matched to a track; this approach is suitable for highly energetic muons ($p_T > 200$ GeV).
Different algorithms are used to assign the momentum to the muon candidate, in order to mitigate the effects of bremsstrahlung, that becomes significant when the muon approaches an energy of the order of 1 TeV. The radiated photons generate spurious hits in the chambers and larger occupancy, significantly deteriorating the momentum measurement.
Starting from 2016 Run, the muon reconstruction takes into account the Alignment Position Errors, namely the uncertainties due to the position of the muon chambers with respect to the silicon detectors. The final resolution on the muon momentum measurement depends on the p_T and η of the candidate, and ranges from 1% for very low momenta, up to $\sim 7\%$ ($|\eta| < 0.9$) – 10% ($1.2 < |\eta| < 2.4$). [DP2016_067]
The muon isolation $I_{\Delta R=0.4}^{\mu}$ is defined similarly to the electron isolation, but by taking into account a larger cone $\Delta R = 0.4$ around the muon direction.

3.2.9.4 Jet reconstruction

The nature of the strong interaction is such that coloured partons, namely quarks and gluons, are forced to aggregate to form a color-neutral hadron, in the process called hadronization. Therefore, partons cannot be observed as free particles in a detector, but rather as collimated jets of hadronic particles.
Jets are reconstructed starting by the PF candidates in the event. The charged hadron subtraction algorithm (CHS) removes candidates not associated to the primary vertex in order to remove contributions from pileup [39]. The remaining particles are used as input to jet clustering algorithms to reconstruct particle-flow jets. The jets are clustered using the FASTJET package [?] with the anti- k_T jet sequential clustering algorithm [40]. A sequential clustering algorithm is designed in order to be infrared and collinear safe, namely, if the final state particles undergo a soft emission or a collinear gluon splitting, the number and shapes of the jets should not change. The starting point of a sequential clustering algorithm is the definition of the distances between two particles i and j , and the distance of a given particle i from the beam-spot B :

$$d_{ij} = \min \left(p_{T,i}^{2a} p_{T,j}^{2a} \right) \frac{R_{ij}^2}{R^2}, \\ d_{iB} = p_{T,i}^{2a} \quad (3.10)$$

where $p_{T(i,j)}$ are the transverse momenta of the particles, $R_{ij}^2 = (y_i - y_j)^2 + (\phi_i - \phi_j)^2$ is the angular distance between the particles, a is an exponent depending on the clustering algorithm chosen, and R is the clustering parameter. The algorithm then operates as follows:

- 868 • it computes all the possible combination of distances d_{ij} and d_{iB} and it finds the mini-
869 mum;
- 870 • if the minimum is d_{ij} , the four-momenta of the particles i and j are summed up in one
871 candidate ij ; i and j are removed from the list of candidates, the distances are updated,
872 and the algorithm proceeds to re-calculate all the possible remaining d_{ij} ;
- 873 • the clustering stops when the smallest quantity is d_{iB} : i particle is defined as one jet,
874 and it is removed from the list of particles;
- 875 • this process is repeated until all the particles are assigned to a jet, that must be separated
876 from another jet at least by a distance $R_{ij} > R$.

877 In case of the anti- k_T algorithm, $\alpha = -1$. It tends to cluster high p_T particles first, since the
878 hard term dominates d_{ij} in equation 3.10. Since the soft particles have lower impacts, the
879 shape of the jet is not sensitive to the soft radiation and rather stable against the softer pile-up
880 contributions.

881 In this analysis, clustering parameters of $R = 0.8$ and $R = 0.4$ will be used to define the
882 “fat”-jets or AK8 jets, and the “standard”-jets or AK4 jets). In order to avoid double-counting
883 of PF candidates, AK4 jets are considered only if the angular separation from the leading AK8
884 jet is larger than $\Delta R > 0.8$.

885 Since the detector response to different particles is not linear, particular care should be taken
886 in the assignment of the measured momentum of the clustered jet to the corresponding true
887 value of the original parton [41]. A set of jet energy corrections (JECs) are applied sequentially
888 and with a fixed order. Each correction consists in a rescaling of the jet four-momentum, and
889 it takes into account different effects that are factorized.

- 890 • The L1 JECs remove the effect of the pile-up; they consist into an offset correction of the
891 jet p_T . They are determined from Monte Carlo (MC) simulations of dijet events produced
892 by strong interaction with and without pile-up events on top, and parametrized as a
893 function of kinematical parameters (jet area, pseudorapidity and p_T) and of the average
894 p_T density per unit area ρ . Residual difference between data and the detector simulation
895 are evaluated in data collected with a random trigger, called zero bias, applying the only
896 requirement of the beam crossing happening. Pile-up offset corrections are displayed in
897 fig. 3.14 (top left), as a function of the jet pseudorapidity.
- 898 • The simulated response of the detector is not uniform over jet p_T and η . This effect is
899 mitigated by the L2L3 MC-truth corrections. They are calculated in MC simulations of
900 dijet events by taking into account the discrepancy between the reconstructed p_T of the
901 jet and the true p_T at particle level, as a function of jet p_T and η . L2L3 scale factors
902 describing the simulated jet response are reported in fig. 3.14 (top right), as a function
903 of the jet pseudorapidity.
- 904 • The small data-MC discrepancies ($\sim 1\%$) left after applying the previous set of JECs are
905 corrected by the L2 and L3 residual corrections. The L2Residuals are calculated in dijet
906 events, as a function of p_T . The L3Residuals are calculated in $Z \rightarrow (\mu\mu, ee) + \text{jet}$ events,
907 photon + jet events and multijet events, as a function of η and p_T , with the p_T -balancing
908 method [41]. Data-MC scale factors for L2L3Residuals are displayed in fig. 3.14 (bottom),
909 as a function of the jet η and p_T .

3.2 CMS detector

- 910 • An optional correction, not used in this analysis, is the L5 flavor-dependent correction,
 911 that is extracted from MC simulations.

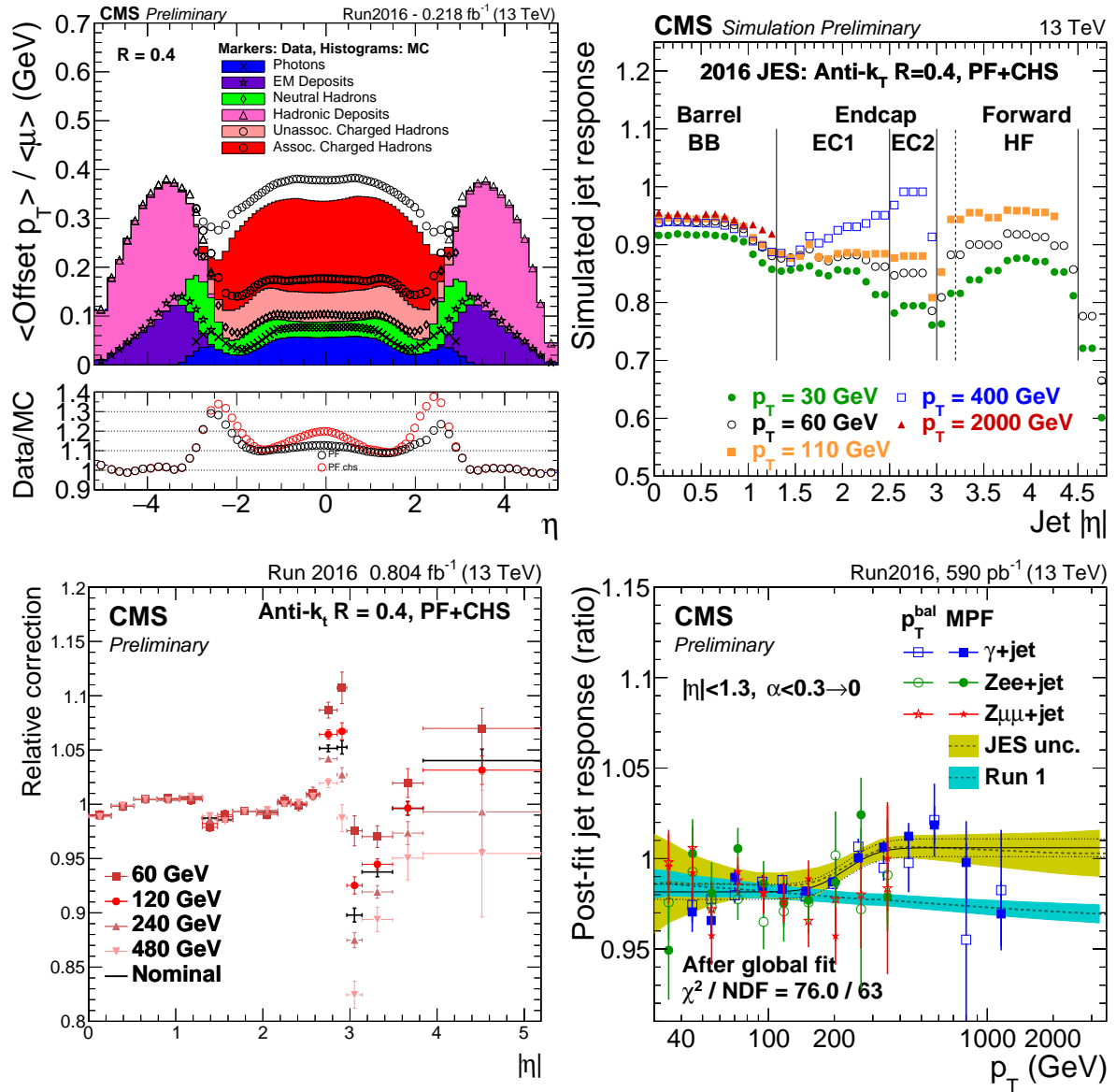


Figure 3.14: Top left: average p_T offset due to additional pile-up events, measured both in data and in MC simulations, as a function of the jet pseudorapidity. Top right: simulated jet response (L2L3 MC-truth corrections), as a function of the jet pseudorapidity. Bottom left: L2L3 residual data-MC corrections, evaluated on dijet events, as a function of the jet η . Bottom right: L2L3 residual data-MC corrections, evaluated on dijet and $Z/\gamma +$ jet events, as a function of the jet p_T .

912 Each jet energy correction is determined with an uncertainty, and reported in fig. 3.15 for 2015
 913 data, as a function of p_T and η of the jet. The total uncertainty for jets with p_T larger than 30
 914 GeV (100 GeV) is smaller than 3% (1%) in the barrel, and up to 5% (3%) in the endcaps.

915 An additional effect that must be taken in account is the discrepancy in the jet energy resolution
 916 (JER) observed in data and in Monte Carlo samples. A smearing procedure is applied in

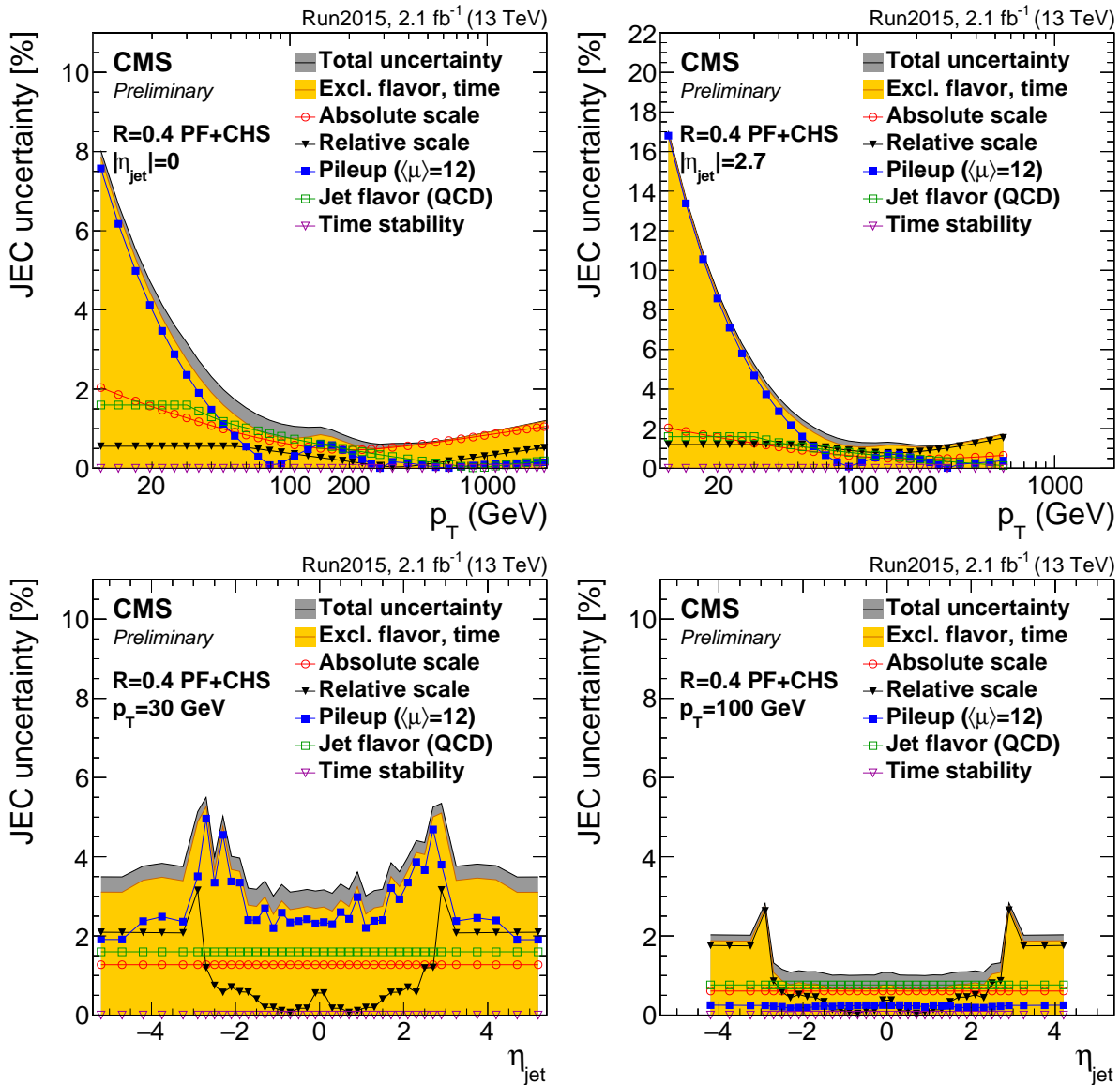


Figure 3.15: Jet energy corrections uncertainties, as a function of jet p_T (top) and η (bottom), calculated in 2015 data. The yellow histograms report the convolution of the uncertainties applied in the analysis.

917 MC simulations (described in detail in sec. 4.2.6), in order to restore a better agreement. Jet
 918 energy resolutions in Monte Carlo simulations are displayed in fig. 3.16 (top), as a function
 919 of the jet p_T and the average number μ of reconstructed primary vertices, considering central
 920 (left) and forward (right) jets. The resolution is stable against the pile-up for jet $p_T > 100$ GeV,
 921 and it ranges from 10% at 100 GeV, down to 4% at 1 TeV. In fig. 3.16 (top). In fig. 3.16 (bottom),
 922 data-MC smearing scale factors are reported as a function of η .

3.2 CMS detector

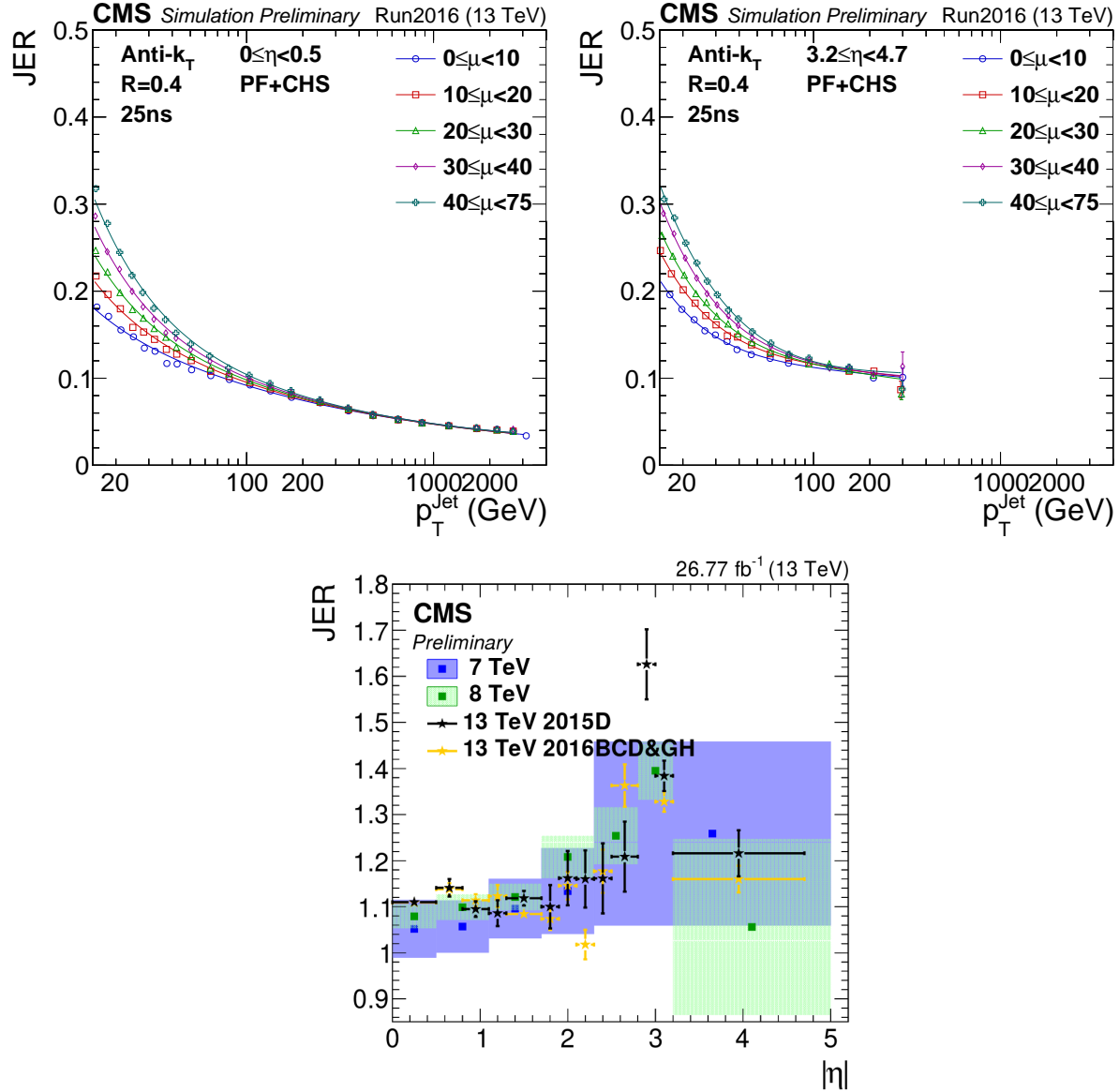


Figure 3.16: Top: jet energy resolution in MC simulations, as a function of the jet p_T . Different curves represent a different average number of primary vertices per event (μ). Bottom: data-MC scale factors, as a function of the jet η , measured in 2016 data (yellow dots).

923 3.2.9.5 Tau reconstruction

924 Tau leptons have a very small lifetime ($\sim 3 \times 10^{-13}$ s), hence they decay before reaching the
 925 pixel detector and they can only be reconstructed through their decay products. Approxima-
 926 tively 60% of the times, τ leptons decay in hadrons, hence they are reconstructed as small
 927 collimated jets in the CMS detector. The main decay modes of the hadronic tau, τ_h , are one
 928 or three charged mesons (mainly π^\pm), also in association with a π^0 decaying in a couple of
 929 photons, and a τ neutrino. Hence, photons and charged hadrons are the main ingredients of
 930 dedicated algorithms to perform the τ_h reconstruction and identification, in order to distin-
 931 guish them from quark and gluon-initiated jets. The main CMS τ_h reconstruction algorithm,

Hadron Plus Strips (HPS) [42], is particle-flow based. HPS builds the tau candidate from a PF jet, clustered with the anti- k_T algorithm with $R = 0.5$, and it reconstructs the $\pi^0 \rightarrow \gamma\gamma$ decays within the jet cone, by taking into account the photon conversions in the silicon detector. The exploitation of the PF informations is such that the HPS algorithm shows stable performances in the reconstruction of the τ_h energy as a function of the energy itself. The τ_h candidate is required to be isolated, namely no energy deposits other than the τ decay products should be present in the tau cone. Depending on the low threshold set to consider the surrounding particles as included in the cone, different isolation working points can be defined. With the looser working point, the probability of misidentifying a quark or gluon jet as a tau is around 1% [42].

3.2.9.6 Missing transverse energy reconstruction

Finally, the presence of neutrinos and other weakly interacting particles can be detected by transverse missing energy (EmissT), defined as the modulus of the vector sum of the transverse momenta of all reconstructed particles.

3.2.9.7 b-quark tagging

3.3 ATLAS, ALICE, LHCb detectors

3.3.1 ATLAS

ATLAS (A Toroidal LHC ApparatuS) is a multi-purpose experiment, that shares the same scientifical aims of CMS. The simultaneous observation of an Higgs boson-like particle at the two experimental facilities represented an irrefutable proof of the discovery of the Higgs boson.

ATLAS has a cylindrical shape (diameter of 25 m, length of 46 m) and weights 7000 tons. Like CMS, ATLAS is composed by many sub-detectors: trackers, calorimeters and muon system. The ATLAS magnetic field is provided by a solenoid, located inside the cylinder, and a big toroid, located outside the sub-detectors, able to reach a magnetic field of 2 T at the interaction point. The main differences among the two experiments are listed below.

- *Tracker* – the CMS tracker has a better p_T resolution (mainly due to the higher magnetic field): $\sigma_{p_T}/p_T \approx 5 \cdot 10^{-4} p_T + 0.01$ at ATLAS; $\sigma_{p_T}/p_T \approx 1.5 \cdot 10^{-4} p_T + 0.005$ at CMS.
- *Electromagnetic calorimeter* – the CMS electromagnetic calorimeter is completely enclosed inside the solenoid, whilst ATLAS calorimeter is outside of the solenoid. The particles going through the solenoid suffer an energy loss and a consequent deterioration of the energy resolution. The CMS ECAL has an enery resolution of $\sigma_E/E \approx 3\%/\sqrt{E}$; the ATLAS calorimeter has a sandwich structure (liquid argon and lead layers) and a resolution of $\sigma_E/E \approx 10\%/\sqrt{E}$.
- *Hadronic calorimeter* – the CMS HCAL is partly inside the solenoid, partly outside, de-pauperating the resolution. The ATLAS hadronic calorimeter (made of iron and plastic scintillator tiles) has an energy resolution $\sigma_E/E \approx 50\%/\sqrt{E} + 0.03$ GeV; CMS HCAL has a resolution of $\sigma_E/E \approx 100\%/\sqrt{E} + 0.05$ GeV.

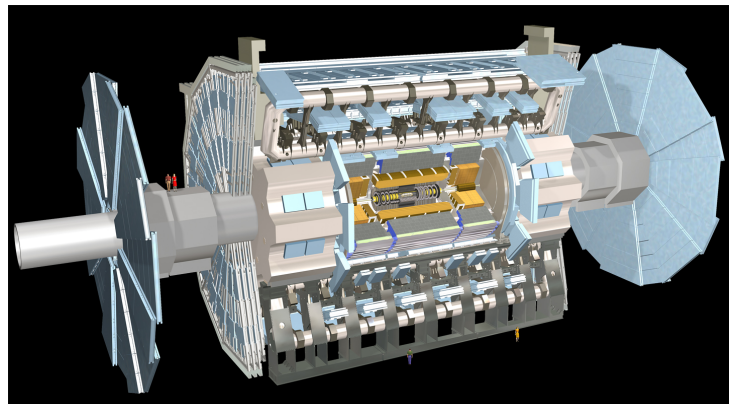


Figure 3.17: The ATLAS experiment.

- 970 • *Muon system* – the peculiar geometry of the ATLAS muon system allows a better resolution
971 of the standalone measurement of the muon momenta (*i.e.*, without using tracker
972 and calorimeters), that is around 10% at 1 TeV. CMS has better performance when com-
973 bining the informations coming from the inner detectors (7% at 1 TeV against the 35%
974 for the standalone measurement).

975 3.3.2 ALICE

976 ALICE (A Large Ion Collider Experiment) studies the heavy ion collisions (lead-lead) or
977 proton-ion in order to explore the physics of the hadrons in high density (or temperature)
978 regimes, when a new state of matter appears, the so-called quark-gluon plasma (QGP). The
979 QGP played a crucial role in the very first instants of life of the universe.

980 3.3.3 LHCb

981 LHCb (Large Hadron Collider beauty) is a detector designed to study the b quark properties,
982 in particular the CP violation and other rare phenomena involved in b hadrons. The final aim
983 of these measurements is trying to solve the matter-antimatter asymmetry problem.

984 The three detectors are depicted in fig. 3.17–3.19.

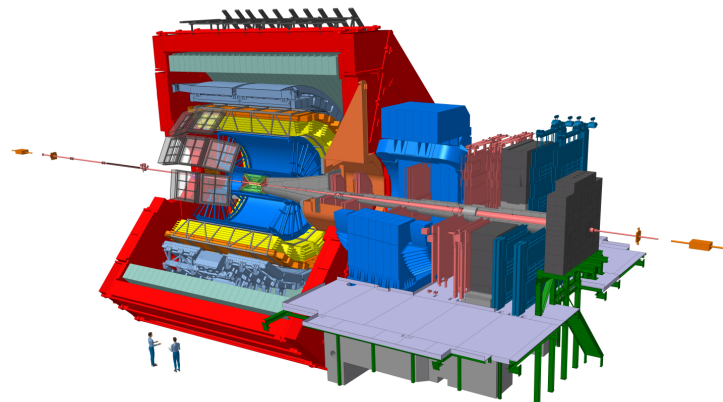


Figure 3.18: The ALICE experiment.

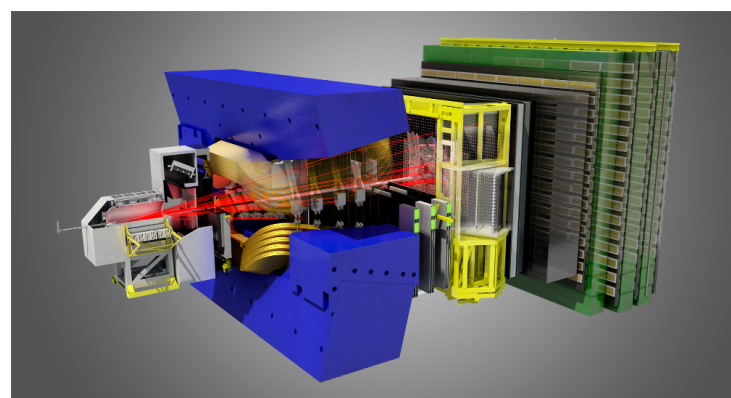


Figure 3.19: The LHCb experiment.

Search for diboson resonances in the $ZV \rightarrow \nu\bar{\nu}q\bar{q}$ final state

988 Brief intro to the analysis

⁹⁸⁹ **4.1 Data and Monte Carlo samples**

4.2 Event selection

4.2 Event selection

In this section, a list of the physics objects used in the analysis is presented, together with performance and validation plots.

The objects are selected according to the standard Run2 recommendations provided by the various POGs for the Summer16 (25ns) MiniAOD-v2 (Moriond recommendations).

The version of CMSSW used for the analysis is CMSSW_8_0_25.

4.2.1 Vertex and Pile-up

How the vertices and pile-up are reconstructed

Due to pileup several primary vertices are typically reconstructed in an event. The primary vertex of the event is defined as the one with the highest sum of transverse momenta $\sum p_T^2$ of clustered physics objects associated to it, which passes the following selections:

- number of degrees of freedom $N_{DoF} > 4$
- vertex position along the beampipe $|z_{vtx}| < 24\text{cm}$
- vertex distance with respect the beam pipe $d_0 < 2\text{cm}$

where z_{vtx} and d_0 are the distance along and perpendicular to the beam line of the vertex with respect the nominal interaction point $(0, 0, 0)$.

The data sample contains a significant number of additional interactions per bunch crossing, an effect known as pileup (PU).

The Summer16 v2 MINIAOD Monte Carlo samples are generated simulating the PU conditions, using the 25ns asymptotic PU scenario. Nevertheless, the MC PU description does not match exactly the conditions in data, and there is therefore the need to reweight the simulated events in order to improve the agreement with the data.

The MC samples are reweighted using the standard CMS PU reweighting technique [43,44] assuming a total inelastic cross section of $\sigma_{in} = 69\,200\mu\text{b}$.

The comparison between the distributions of primary vertices in data and MC after the PU reweighting is applied is shown in Figure 4.1 for an event selection (called inclusive selection) requiring large amount of E_T^{miss} recoiling against an AK8 fat jet (Tab. ??).

Figure 4.1: Primary vertices distributions after reweighting with the official recipe and $\sigma_{in} = 69\,200\mu\text{b}$.

4.2.2 Electrons

How the electrons are reconstructed: The electron identification variables that have been found to be the most powerful, and are used in the selection, are: the energy-momentum match between the seed cluster and the trackE seed/pin, the variables measuring spatial matching between the track and the supercluster, in and in, the supercluster width,i i(as taken from the covariance matrix using logarithmic weights), and the hadronic leakage variable H/E. The supercluster width is to a very good approximation unaffected by the spreading due to the magnetic field of the showering in the tracker material.

Isolation variables are computed in three sub-detectors: the tracker, the ECAL, and the HCAL.

1026 Transverse energy/momentum sums are evaluated in regions of $R < 0.3$. As electrons undergo
 1027 bremsstrahlung energy loss in the tracker material, care is taken to remove from the isolation
 1028 sums the contributions from bremsstrahlung photons and possible resulting conversion
 1029 electrons.

1030 Electrons are reconstructed from energy deposits in the ECAL matched to tracks recon-
 1031 structed in the silicon tracker. The electron trajectories are reconstructed using a dedicated
 1032 modeling of the electron energy loss and fitted with a Gaussian sum filter. Electrons used in
 1033 this analysis are required to pass the Particle Flow criteria, and to fall in the ECAL pseudora-
 1034 pidity fiducial range ($|\eta| < 2.5$).

1035 The electron identification used in this analysis is based on the “cut-based” Id defined
 1036 by the EGamma POG for the Summer16 25ns [45], and suggested also for the usage in 80X
 1037 for the so-called Moriond dataset. Isolation cuts are already applied within the cut-based
 1038 Id definitions, therefore no additional Isolation cut is required. In the isolation definition
 1039 the effect of PU is considered by taking into account the energy deposits in the calorimeter,
 1040 estimated through the so-called ρ -area method, by subtracting the median energy density in
 1041 the event ρ multiplied by electron effective area. The isolation value is computed in a ΔR cone
 1042 of 0.3 centered along the lepton direction.

1043 Since in this analysis we are aiming at a final state without any lepton, every electron
 1044 identified with *veto* cut-based Id, transverse momentum $p_T > 10$ GeV is vetoed. The detailed
 1045 set of cuts to define a *veto* cut-based Id electron are reported in the Table 4.1.

Electrons	Veto	
	EB	EE
$\sigma_{i\eta i\eta}$	<	0.0115
$\Delta\eta_{in}^{seed}$	<	0.00749
$\Delta\varphi_{in}$	<	0.228
H/E	<	0.356
rellIso (EA)	<	0.175
$ 1/E - 1/p $	<	0.299
$ d_0 $	<	0.05
$ d_z $	<	0.10
missing hits	\leq	2
conversion veto	yes	yes

Table 4.1: Summer16 cut-based selection for 25ns conditions. EB: barrel cuts ($|\eta_{\text{supercluster}}| \leq 1.479$); EE: endcap cuts ($|\eta_{\text{supercluster}}| > 1.479$)

1046 Scale factors for electron identification (including isolation) are provided by Egamma POG,
 1047 derived for 80X (Moriond 17 recommendation), that can be found in [46].

1048 4.2.3 Muons

1049 How the muons are reconstructed

1050 In the standard CMS reconstruction for pp collisions, muon tracks are first reconstructed
 1051 independently in the inner tracker (tracker track) and in the muon system (standalone-muon
 1052 track). Based on these objects, two reconstruction approaches are used [47]: *Global Muon*
 1053 (*outside-in*) and *Tracker Muon* (*inside-out*).

4.2 Event selection

reconstruction (*outside-in*): for each standalone-muon track, a matching tracker track is found by comparing parameters of the two tracks propagated onto a common surface, and a global-muon track is fitted combining hits from the tracker track and standalone-muon track, using the Kalman-filter technique [48]. At large transverse momenta, $p_T > 200\text{GeV}$, the global-muon fit can improve the momentum resolution compared to the tracker-only fit.

reconstruction (*inside-out*): in this approach, all tracker tracks with $p_T > 0.5\text{GeV}$ and the total momentum $p > 2.5\text{GeV}$ are considered as possible muon candidates and are extrapolated to the muon system taking into account the magnetic field, the average expected energy losses, and multiple scattering in the detector material. If at least one muon segment (i.e., a short track stub made of DT or CSC hits) matches the extrapolated track, the corresponding tracker track qualifies as a Tracker Muon.

Tracker Muon reconstruction is more efficient than the Global Muon reconstruction at low momenta, $p_T \lesssim 5\text{GeV}$, because it requires only a single muon segment in the muon system, whereas Global Muon reconstruction is designed to have high efficiency for muons penetrating through more than one muon station and typically requires segments in at least two muon stations. Thanks to the high tracker-track efficiency and a very high efficiency of reconstructing segments in the muon system, about 99% of muons produced in pp collisions and having sufficiently high momentum are reconstructed either as a Global Muon or a Tracker Muon, and very often as both. Muons reconstructed only as standalone-muon tracks have worse momentum resolution and less favorable collision muon to cosmic-ray muon ratio than the Global and Tracker Muons and are usually not used in physics analyses.

Muons are usually based on the *Particle Flow Muon* selection, considering Global Muon or a Tracker Muon candidates and by applying minimal requirements on the track components in the muon system and taking into account a matching with small energy deposits in the calorimeters.

For muons reconstructed using the PF algorithm, the standard muon isolation is defined as the ratio of the p_T sum of all charged and neutral particle-flow candidates in the event within a cone with a radius of $\Delta R = 0.4$ centered along the lepton direction. Corrections in order to reduce the PU contamination are also applied, using the $\Delta\beta$ method. Charged candidates falling into the cone that are not compatible with the primary vertex are removed from the sum. Additionally, the neutral contribution from PU is estimated to be half the one coming from charged candidates, and this quantity is also subtracted from the total. Eventually, the scalar sum is divided by the lepton p_T itself. The general formula for the standard *particle-flow* isolation is then:

$$I_{rel} = \left[\sum p_T^{\text{ch had}} + \max(\sum p_T^{\text{neu had}} + \sum p_T^\gamma - 0.5 \cdot \sum p_T^{\text{pu ch had}}, 0) \right] / p_T^\ell$$

where $\sum p_T^{\text{ch had}}$ is the sum of the transverse momenta of the charged hadrons, $\sum p_T^{\text{neu had}}$ is the sum of transverse energies of the neutral hadrons, p_T^γ is the sum of the transverse energy of particle flow photons and $\sum p_T^{\text{pu ch had}}$ is the sum of transverse momenta of the charged particles in the cone of interest but with particles not originating from the primary vertex (for pileup corrections).

In the VZ event selection, all muons identified with the Loose standard id, p_T over 10 GeV, PF isolation below 0.25, $|\eta| < |2.4|$ are vetoed.

Scale factors for muon identification and isolation are centrally provided as a function of the muon p_T and η by the Muon POG [49], and are applied consistently in the analysis.

 1088 **4.2.4 Taus**

 1089 **How the taus are reconstructed**

1090 The presence of hadronically-decaying taus only act as veto for the events both in the sig-
 1091 nal and in the control regions to suppress electroweak backgrounds. The selection criteria
 1092 for taus are $p_T > 18$ GeV and $|\eta| < 2.3$. The Run2 TauPOG recommended identification cri-
 1093 teria [50] (`decayModeFinding`, `byLooseCombinedIsolationDeltaBetaCorr3Hits`) are required
 1094 and applied in order to identify possible tau candidates.

 1095 **4.2.5 Photons**

 1096 **How the photons are reconstructed**

1097 As in the case of tau leptons, a photon veto is applied in the analysis both for the signal
 1098 and the control regions. Events are rejected if they contains one (or more) photon with $p_T > 15$
 1099 GeV, $|\eta| < 2.5$, passing the Loose cut-based photon ID. The Loose photon Id is applied as
 1100 in the EGamma POG recommendations for Run2 analyses [51] (tuned on Spring16 25 ns
 1101 samples). The isolation cuts (using the rho-area method for the mitigation of the pileup) and
 1102 conversion safe electron veto are applied. The isolation value is computed in a ΔR cone of
 1103 0.3 and is corrected for pileup by subtracting the event-by-event energy density (ρ) times an
 1104 effective area. The applied cut-based definition of the Loose photon Id is reported in Table 4.2.

Photons	Loose	
	EB	EE
H/E	<	0.0597
$\sigma_{i\eta i\eta}$	<	0.01031
PF ch.had.iso.(ρ -corr)	<	1.295
PF neu.had.iso.(ρ -corr)	<	$10.910 + 0.0148p_T + 0.000017p_T^2$
PF photon iso.(ρ -corr)	<	$5.931 + 0.0163p_T + 0.000014p_T^2$
conversion veto	yes	yes

Table 4.2: Photon cut-based Id for Spring16 25ns conditions. EB: barrel cuts ($|\eta_{\text{supercluster}}| \leq 1.479$); EE: endcap cuts ($|\eta_{\text{supercluster}}| > 1.479$)

1105

1106 Scale factors for photon identification (including isolation) are provided by Egamma POG,
 1107 derived for 80X (Moriond 17 recommendation), that can be found in [46].

4.2 Event selection

4.2.6 Jets

How the jets are reconstructed

The latest jet energy corrections are applied to AK4 and AK8 CHS jets, and the tags are Summer16 23Sep2016V3.

In this analysis, jets are considered if the corrected p_T is larger than 30 GeV for AK4 jets and 200GeV for AK8 jets, and lie in the tracker acceptance ($|\eta| < 2.4$). Additionally, AK4 are required to pass *loose* jet identification requirements, AK8 are required to pass *tight* jet identification requirements defined by the JETMET POG for Run2 analyses [52], listed in Table 4.3. AK8 jets are used to reconstruct the hadronically decaying electroweak boson candidate, whilst AK4 jets are used to suppress the contribution of top and QCD background events.

1119

EFFICIENZA di TIGHT ID?

1121

Figure 4.2- 4.4 show the data/simulation comparison after the analysis selections (Tab. ?? without Top cleaning and Event cleaning).

PF Jet ID	loose	tight
Neutral Hadron Fraction	< 0.99	< 0.90
Neutral EM Fraction	< 0.99	< 0.90
Number of Constituents	> 1	> 1
Muon Fraction	-	-
Additionally, for $ \eta < 2.4$		
Charged Hadron Fraction	> 0	> 0
Charged Multiplicity	> 0	> 0
Charged EM Fraction	< 0.99	< 0.99

Table 4.3: *Loose* and *Tight* jet identification requirements for Run2 (Spring16) 25ns conditions.

Figure 4.2: Number of reconstructed AK8 jets after selections.

Figure 4.3: Leading AK8 jet p_T spectra after selections.

Figure 4.4: Leading AK8 jet η spectra after selections.

Since it has been measured that the jet energy resolution (JER) is not the same in data and MC, an additional smearing is applied in simulation, in order to get a better agreement, as suggested by JETMET POG [53].

There are two independent ways to get the smearing. With the scaling method, corrected four-momentum of a reconstructed jet is rescaled with a factor

$$c_{\text{JER}} = 1 + (s_{\text{JER}} - 1) \frac{p_T - p_T^{\text{ptcl}}}{p_T},$$

where p_T is its transverse momentum, p_T^{ptcl} is the transverse momentum of the corresponding jet clustered from generator-level particles, and s_{JER} is the data-to-simulation core resolution scale factor. Factor c_{JER} is truncated at zero, i.e. if it is negative, it is set to zero. This method only works if a well-matched particle-level jet is present and can result in a large shift of the response otherwise. The following requirements are imposed for the matching:

$$\Delta R < R_{\text{cone}}/2, |p_T - p_T^{\text{ptcl}}| < 3\sigma_{\text{JER}} p_T.$$

- 1127 Here R_{cone} is the jet cone size parameter (for instance, 0.4 for AK4 jets) and σ_{JER} is the relative
 1128 p_T resolution as measured in simulation.

An alternative approach, which does not require the presence of a matching particle-level jet, is the stochastic smearing. In this case corrected jet four-momentum is rescaled with a factor

$$c_{\text{JER}} = 1 + \mathcal{N}(0, \sigma_{\text{JER}}) \sqrt{\max(s_{\text{JER}}^2 - 1, 0)},$$

- 1129 where σ_{JER} and s_{JER} are the relative p_T resolution in simulation and data-to-simulation scale
 1130 factors, and $\mathcal{N}(0, \sigma)$ denotes a random number sampled from a normal distribution with a
 1131 zero mean and variance σ^2 . As before, scaling factor c_{JER} is truncated at zero. This method
 1132 only allows to degrade the resolution.

- 1133 The smearing procedure adopted in this analysis is the hybrid method: when matching
 1134 particle-level jet is found, the scaling method is used; otherwise the stochastic smearing is
 1135 applied. The smearing coefficients and their errors, provided by JETMET POG, are reported
 1136 in Tab. 4.4 for 2016 data (tag: Spring1625nsV10).

Jet η	SF
0.0 – 0.5	1.109 ± 0.008
0.5 – 0.8	1.138 ± 0.013
0.8 – 1.1	1.114 ± 0.013
1.1 – 1.3	1.123 ± 0.024
1.3 – 1.7	1.084 ± 0.011
1.7 – 1.9	1.084 ± 0.011
1.9 – 2.1	1.140 ± 0.047
2.1 – 2.3	1.067 ± 0.053
2.3 – 2.5	1.177 ± 0.041
2.5 – 2.8	1.364 ± 0.039
2.8 – 3.0	1.857 ± 0.071
3.0 – 3.2	1.328 ± 0.022
3.2 – 5.0	1.16 ± 0.029

Table 4.4: Smearing coefficients and JER uncertainties.

4.2 Event selection

4.2.7 Jet mass

The jet mass is the main observable in distinguishing a V-jet from a QCD jet. Jet grooming consists in the suppression of uncorrelated UE/PU (underlying event and pile-up) radiation from the target jet and improves the discrimination pushing the jet mass for QCD jets towards lower values while maintaining the jet mass for V-jets around the boson-mass.

The grooming algorithm considered in this analysis is the following:

Soft-drop: The “soft drop declustering” is a jet substructure technique which recursively removes soft wide-angle radiation from a jet [54]. The soft drop algorithm depends on two parameters: a soft threshold z_{cut} and an angular exponent β . Like any grooming method, soft drop declustering removes wide-angle soft radiation from a jet in order to mitigate the effects of contamination from initial state radiation (ISR), underlying event (UE), and multiple hadron scattering (pileup). Given a jet of radius R_0 with only two constituents, the soft drop procedure removes the softer constituent unless:

$$\frac{\min(p_T^1, p_T^2)}{p_T^1 + p_T^2} > z_{cut} \left(\frac{\Delta R_{12}}{R_0} \right)^\beta$$

By construction, this condition fail for wide-angle soft radiation. The degree of jet grooming is controlled by z_{cut} and β , with $\beta \rightarrow \infty$ returning back an ungroomed jet. The $\beta = 0$ limit of the energy loss is particularly interesting, since it is largely insensitive to the value of the strong coupling constant. The default parameters used by CMS are $\beta = 0$ and $z_{cut} = 0.1$.

The grooming algorithm, **soft-drop**, is used in association with **PUPPI** in order to remove soft and wide-angle radiations and the pile-up contribution. It is a shared choice among all the diboson analyses, praised by theoreticians.

Unfortunately, the default soft-drop + PUPPI jet mass suffers from a systematic shift from the expected value of about $\sim 10\%$, and some residual dependence on the jet p_T . Further corrections to the jet mass have been applied:

Gen: a p_T -dependent correction to account for a small shift in the generated vector boson mass, applied only on simulated samples

Reco: a p_T -dependent correction to the reconstructed jet mass, applied separately for jets in the barrel and endcaps regions

These corrections are evaluated centrally by JMAR and documented in [55], and applied accordingly within the analysis.

Figure 4.6- 4.7 show the jet mass for W or Z bosons before and after the correction, without applying any cut on this variable.

Figure 4.5: Softdrop + PUPPI mass of AK8 jet reconstructed for different bulk graviton signal samples; left: before corrections. right: after corrections.

Furthermore, in order to obtain a better data-Monte Carlo agreement, a smearing procedure has been applied to the puppi softdrop mass, by using the stochastic method, with a constant smearing coefficient provided by JETMET POG (1.00 ± 0.20), that does not depend on jet pseudorapidity if it is restricted to $|\eta| < 2.5$.

Figure 4.6: Softdrop + PUPPI mass of AK8 jet reconstructed for different W' signal samples; left: before corrections. right: after corrections.

Figure 4.7: Softdrop + PUPPI mass of AK8 jet; left: before corrections. right: after corrections.

1166 4.2.8 Jet substructure

In order to further discriminate signal from background, it is useful to investigate the inner structure of the jet. Studying the distribution of the jet constituents with respect to the jet axis allows us to test the hypothesis of the existence of multiple substructures, that could be evidence of jets originated by more than one parton. This procedure proceeds as follows: the constituents of the jet are clustered again with the k_T algorithm, however the procedure is stopped when one obtains N subjets. Then, a new variable, the N-subjettiness, is introduced. It is defined as:

$$\tau_N = \frac{1}{d_0} \sum_k p_{T,k} \min(\Delta R_{1,k}^\beta, \Delta R_{2,k}^\beta, \dots, \Delta R_{N,k}^\beta)$$

1167 where β is an arbitrary parameter, the index k runs over the jet constituents and the distances
1168 $\Delta R_{N,k}$ are calculated with respect to the axis of the N-th subjet, obtained by one iteration of τ
1169 minimization by varying the subjet axes around the k_T subjet axes.

The normalization factor d_0 is calculated as $d_0 = \sum_k p_{T,k} R_0^\beta$, setting R_0 to the radius of the original jet. The N-subjettiness is always included in the interval from 0 to 1 and represents the compatibility of the jet structure with an N-subjet hypothesis: small values correspond to high compatibility. Indeed, τ_N weights the transverse momentum of the jet constituents by their angular distance to the closest subjet. In this analysis the N-subjettiness is calculated from the ungroomed jet with the parameter $\beta = 1$. The subjettiness related to the one and two subjet hypothesis is thus:

$$\tau_1 = \frac{1}{d_0} \sum_k p_{T,k} \Delta R_{1,k}$$

and

$$\tau_2 = \frac{1}{d_0} \sum_k p_{T,k} \min(\Delta R_{1,k}, \Delta R_{2,k})$$

1170 In principle, these two quantities should allow us to distinguish the dipole-like nature of the
1171 showering of the Higgs decay from the classic monopole structure of QCD jets. In particular,
1172 the variable that best discriminates between V-jets and QCD jets is the ratio of 2-subjettiness
1173 and 1-subjettiness, $\tau_{21} = \tau_2 / \tau_1$.

1174 Figure 4.8 shows the τ_{21} distributions for the PUPPI algorithm.

Figure 4.8: τ_{21} subjettiness of PUPPI AK8 jet after inclusive selections.

4.2 Event selection

4.2.9 b-tagging

B-tagging algorithms are applied to both the fat-jet and the sub-jets, independently. For sub-jets, run-II taggers are by default applied on the same charged particle-flow candidate list that is used in the jet clustering (*explicit jet-to-track association*). Thanks to the explicit jet-to-track association, the two sub-jets do not share any PF-constituent, avoiding unintended correlations.

The jet or sub-jet is considered as tagged if the discriminator value is above some threshold value, often referred to as the cut value, and the efficiency is defined as the number of jets which have a discriminator value that is above that cut divided by the total number of jets (of the same flavor).

The b-tagging algorithm used to set the analysis strategy is the Combined Secondary Vertex (CSV) [56] discriminator (full name `pfCombinedInclusiveSecondaryVertexV2BJetTags`). Different working points are provided by the POG for Run2 analyses [57], as shown in table 4.2.9, but the only one used in this analysis is the *loose* working point.

Working point	CSV cut	mis-tag probability
CSVL (Loose)	> 0.5426	$\approx 10\%$
CSVM (Medium)	> 0.8484	$\approx 1\%$
CSVT (Tight)	> 0.9535	$\approx 0.1\%$

Table 4.5: Working point for CSV b-tagging algorithm.

B-tagging efficiency is not the same in data and MC. In order to take into account this difference, the BTV POG provides collections of b-tagging scale factors for b-jets and mistagged light jets, measured for different physics processes, for the supported tagging algorithms and the three standard working points [56]. A weight is calculated on a per-event basis as a function of the b-tagging status of the jets and their kinematic variables [58].

In this analysis, b-tagging is used in order to reject events where a top quark is involved, by asking to the AK4 jets not laying in the AK8 jet cone to be anti b-tagged (in practice, the maximum CSV value allowed is the loose working point, CSVL).

4.2.10 Missing Energy

How the MET is reconstructed

The E_T^{miss} is the imbalance in the transverse momentum of all visible particles, and it is reconstructed with the particle flow algorithm [59]. The raw E_T^{miss} is defined as the inverse vectorial sum of the transverse momentum of all the reconstructed charged and neutral particle flow candidates: $E_T^{\text{miss}} = - \sum_{i=0}^{\text{all}} \vec{p}_{T,i}$. The raw E_T^{miss} is systematically different from true E_T^{miss} , for many reasons including the non-compensating nature of the calorimeters and detector misalignment. To better estimate the true E_T^{miss} , corrections can be applied:

Type-0: a mitigation for the degradation of the E_T^{miss} reconstruction due to the pileup interactions, by applying the CHS algorithm. However, the E_T^{miss} contribution from pileup neutral particles cannot be easily subtracted; the assumption is that the E_T^{miss} contribution term of charged and neutral pileup particles are the same, and cancellation at the true level is exact: $\sum_{\text{neuPU}} \vec{p}_{T,i}^{\text{true}} + \sum_{\text{chPU}} \vec{p}_{T,i}^{\text{true}} = 0$. An additional E_T^{miss} term is then added to the raw E_T^{miss} to take into account the neutral PU contribution, which is equal

1211 to the charged one with a multiplicative scale factor taking into account calorimeter
 1212 mismeasurements of low- p_T energy deposits.

1213 *Type-1*: propagation of the jet energy corrections (JEC) to MET. The Type-I correction replaces
 1214 the vector sum of transverse momenta of particles which can be clustered as jets with
 1215 the vector sum of the transverse momenta of the jets to which JEC is applied.

1216 Particle flow E_T^{miss} with type-1 corrections applied is currently the default one used by CMS
 1217 physics analyses. Additionally, some E_T^{miss} filters have been recommended by JETMET POG
 1218 for Run2 analyses [52], in order to remove events with spurious E_T^{miss} related to detector noise
 1219 and bad reconstructions, and they are listed in sec. ??.

1220 Since the E_T^{miss} corrections and uncertainties depend on the JEC applied, they are re-
 1221 computed accordingly following the JETMETPOG recommendation:

```
1222 from PhysicsTools.PatUtils.tools.runMETCorrectionsAndUncertainties import
1223 runMetCorAndUncFromMiniAOD
1224 # If you only want to re-correct and get the proper uncertainties
1225 runMetCorAndUncFromMiniAOD(process,
1226                         isData=True (or False),
1227                         )
1228 process.p = cms.Path(process.fullPatMetSequence *
1229 process.yourAnalyzer)
1230
1231 cms.InputTag("slimmedMETS", "", "YourProcessName")
```

1232 Figure 4.9 show the E_T^{miss} distribution for data and Monte Carlo after the corrections and
 1233 filters.

Figure 4.9: Type-1 corrected E_T^{miss} distribution after inclusive selections.

4.3 Diboson candidate reconstruction

1234 4.3 Diboson candidate reconstruction

₁₂₃₅ **4.4 Background estimation**

4.5 Systematic uncertainties

1236 4.5 Systematic uncertainties

₁₂₃₇ **4.6 Results**

Combination of diboson searches in semileptonic final states

1241

Chapter

6

Conclusions

1242

1243

1244

Bibliography

1245

1246

- 1247 [1] G. Aad *et al.*, "Observation of a new particle in the search for the Standard Model Higgs
1248 boson with the ATLAS detector at the LHC," *Phys. Lett. B*, vol. 716, p. 1, 2012.
- 1249 [2] S. Chatrchyan *et al.*, "Observation of a new boson at a mass of 125 GeV with the CMS
1250 experiment at the LHC," *Phys. Lett. B*, vol. 716, p. 30, 2012.
- 1251 [3] S. Chatrchyan *et al.*, "Observation of a new boson with mass near 125 GeV in pp collisions
1252 at $\sqrt{s} = 7$ and 8 TeV," *JHEP*, vol. 06, p. 081, 2013.
- 1253 [4] G. Aad *et al.*, "Evidence for the spin-0 nature of the Higgs boson using ATLAS data,"
1254 *Phys. Lett. B*, vol. 726, p. 120, 2013.
- 1255 [5] V. Khachatryan *et al.*, "Precise determination of the mass of the Higgs boson and tests of
1256 compatibility of its couplings with the standard model predictions using proton collisions
1257 at 7 and 8 TeV," *Eur. Phys. J. C*, vol. 75, p. 212, 2015.
- 1258 [6] G. Aad *et al.*, "Measurement of the Higgs boson mass from the $H \rightarrow \gamma\gamma$ and $H \rightarrow ZZ^* \rightarrow$
1259 4ℓ channels in pp collisions at center-of-mass energies of 7 and 8 TeV with the ATLAS
1260 detector," *Phys. Rev. D*, vol. 90, p. 052004, 2014.
- 1261 [7] CMS and ATLAS Collaborations, "Combined Measurement of the Higgs Boson Mass in
1262 pp Collisions at $\sqrt{s} = 7$ and 8 TeV with the ATLAS and CMS Experiments." Submitted
1263 to *Phys. Rev. Lett.*, 2015.
- 1264 [8] G. Degrassi, S. Di Vita, J. Elias-Miro, J. R. Espinosa, G. F. Giudice, G. Isidori, and A. Stru-
1265 mua, "Higgs mass and vacuum stability in the Standard Model at NNLO," *JHEP*, vol. 08,
1266 p. 098, 2012.
- 1267 [9] D. Pappadopulo, A. Thamm, R. Torre, and A. Wulzer, "Heavy vector triplets: bridging
1268 theory and data," *Journal of High Energy Physics*, vol. 2014, no. 9, pp. 1–50, 2014.
- 1269 [10] V. D. Barger, W.-Y. Keung, and E. Ma, "A Gauge Model With Light W and Z Bosons,"
1270 *Phys. Rev.*, vol. D22, p. 727, 1980.

- 1271 [11] C. Grojean, E. Salvioni, and R. Torre, "A weakly constrained W' at the early LHC," *JHEP*,
1272 vol. 07, p. 002, 2011.
- 1273 [12] R. Contino, D. Pappadopulo, D. Marzocca, and R. Rattazzi, "On the effect of resonances
1274 in composite higgs phenomenology," *Journal of High Energy Physics*, vol. 2011, no. 10,
1275 pp. 1–50, 2011.
- 1276 [13] B. Bellazzini, C. Csáki, and J. Serra, "Composite Higgses," *Eur. Phys. J.*, vol. C74, no. 5,
1277 p. 2766, 2014.
- 1278 [14] G. F. Giudice, C. Grojean, A. Pomarol, and R. Rattazzi, "The Strongly-Interacting Light
1279 Higgs," *JHEP*, vol. 06, p. 045, 2007.
- 1280 [15] A. Wulzer, "An Equivalent Gauge and the Equivalence Theorem," *Nucl. Phys.*, vol. B885,
1281 pp. 97–126, 2014.
- 1282 [16] A. M. Sirunyan *et al.*, "Search for massive resonances decaying into WW, WZ, ZZ, qW,
1283 and qZ with dijet final states at $\sqrt{s} = 13$ TeV," 2017.
- 1284 [17] CMS Collaboration, "Search for massive resonances decaying into WW, WZ, ZZ, qW and
1285 qZ in the dijet final state at $\sqrt{s} = 13$ TeV," CMS Physics Analysis Summary CMS-PAS-
1286 B2G-17-001, CERN, Geneva, 2017.
- 1287 [18] C. Collaboration, "Search for heavy resonances decaying into a vector boson and a Higgs
1288 boson in hadronic final states with 2016 data," 2017.
- 1289 [19] CMS Collaboration, "Search for heavy resonances decaying into a vector boson and a
1290 Higgs boson in hadronic final states with 2016 data," CMS Physics Analysis Summary
1291 CMS-PAS-B2G-17-002, CERN, Geneva, 2017.
- 1292 [20] CMS Collaboration, "Search for heavy resonances decaying into a Z boson and a W
1293 boson in the $\ell^+\ell^-q\bar{q}$ final state," CMS Physics Analysis Summary CMS-PAS-B2G-16-022,
1294 CERN, Geneva, 2017.
- 1295 [21] V. Khachatryan *et al.*, "Search for heavy resonances decaying into a vector boson and a
1296 Higgs boson in final states with charged leptons, neutrinos, and b quarks," *Phys. Lett.*,
1297 vol. B768, pp. 137–162, 2017.
- 1298 [22] CMS Collaboration, "Search for new resonances decaying to $WW/WZ \rightarrow \ell\nu qq$," CMS
1299 Physics Analysis Summary CMS-PAS-B2G-16-020, CERN, Geneva, 2016.
- 1300 [23] CMS Collaboration, "Search for heavy resonances decaying into a Z boson and a vector
1301 boson in the $\nu\nu q\bar{q}$ final state," CMS Physics Analysis Summary CMS-PAS-B2G-17-005,
1302 CERN, Geneva, 2017.
- 1303 [24] M. Aaboud *et al.*, "Search for diboson resonances with boson-tagged jets in pp collisions
1304 at $\sqrt{s} = 13$ TeV with the ATLAS detector," 2017.
- 1305 [25] ATLAS Collaboration, "Search for WW/WZ resonance production in $\ell\nu qq$ final states in
1306 pp collisions at $\sqrt{s} = 13$ TeV with the ATLAS detector," ATLAS Conference Note ATLAS-
1307 CONF-2017-051, CERN, Geneva, Jul 2017.

BIBLIOGRAPHY

- 1308 [26] “Searches for heavy ZZ and ZW resonances in the llqq and vvqq final states in pp col-
1309 lisions at $\text{sqrt}(s) = 13 \text{ TeV}$ with the ATLAS detector,” ATLAS Conference Note ATLAS-
1310 CONF-2016-082, CERN, Geneva, Aug 2016.
- 1311 [27] M. Aaboud *et al.*, “Search for heavy resonances decaying to a W or Z boson and a Higgs
1312 boson in the $q\bar{q}^{(\prime)} b\bar{b}$ final state in pp collisions at $\sqrt{s} = 13 \text{ TeV}$ with the ATLAS detector,”
1313 2017.
- 1314 [28] ATLAS Collaboration, “Search for heavy resonances decaying to a W or Z boson and a
1315 Higgs boson in final states with leptons and b -jets in 36.1 fb^{-1} of pp collision data at
1316 $\sqrt{s} = 13 \text{ TeV}$ with the ATLAS detector,” ATLAS Conference Note ATLAS-CONF-2017-
1317 055, CERN, Geneva, Jul 2017.
- 1318 [29] L. Randall and R. Sundrum, “A Large mass hierarchy from a small extra dimension,”
1319 *Phys. Rev. Lett.*, vol. 83, pp. 3370–3373, 1999.
- 1320 [30] L. Randall and R. Sundrum, “An Alternative to compactification,” *Phys. Rev. Lett.*, vol. 83,
1321 pp. 4690–4693, 1999.
- 1322 [31] K. Agashe, H. Davoudiasl, G. Perez, and A. Soni, “Warped Gravitons at the LHC and
1323 Beyond,” *Phys. Rev.*, vol. D76, p. 036006, 2007.
- 1324 [32] A. L. Fitzpatrick, J. Kaplan, L. Randall, and L.-T. Wang, “Searching for the Kaluza-Klein
1325 Graviton in Bulk RS Models,” *JHEP*, vol. 09, p. 013, 2007.
- 1326 [33] H. Davoudiasl, J. L. Hewett, and T. G. Rizzo, “Phenomenology of the Randall-Sundrum
1327 Gauge Hierarchy Model,” *Phys. Rev. Lett.*, vol. 84, p. 2080, 2000.
- 1328 [34] T. Gherghetta and A. Pomarol, “Bulk fields and supersymmetry in a slice of AdS,” *Nucl.*
1329 *Phys.*, vol. B586, pp. 141–162, 2000.
- 1330 [35] H. Davoudiasl, J. L. Hewett, and T. G. Rizzo, “Experimental probes of localized gravity:
1331 On and off the wall,” *Phys. Rev.*, vol. D63, p. 075004, 2001.
- 1332 [36] A. Oliveira, “Gravity particles from Warped Extra Dimensions, predictions for LHC,”
1333 2014.
- 1334 [37] CMS Collaboration, “Search for diboson resonances in the $2l2\nu$ final state,” CMS Physics
1335 Analysis Summary CMS-PAS-B2G-16-023, CERN, Geneva, 2017.
- 1336 [38] CMS Collaboration, “Search for heavy resonances decaying to a pair of Higgs bosons in
1337 the four b quark final state in proton-proton collisions at $\sqrt{s} = 13 \text{ TeV}$,” CMS Physics
1338 Analysis Summary CMS-PAS-B2G-16-026, CERN, Geneva, 2017.
- 1339 [39] “Pileup Removal Algorithms,” Tech. Rep. CMS-PAS-JME-14-001, CERN, Geneva, 2014.
- 1340 [40] M. Cacciari, G. P. Salam, and G. Soyez, “The anti- k_t jet clustering algorithm,” *JHEP*,
1341 vol. 04, p. 063, 2008.
- 1342 [41] T. C. collaboration, “Determination of jet energy calibration and transverse momentum
1343 resolution in cms,” *Journal of Instrumentation*, vol. 6, no. 11, p. P11002, 2011.

- 1344 [42] S. Chatrchyan *et al.*, “Performance of tau-lepton reconstruction and identification in
1345 CMS,” *JINST*, vol. 7, p. P01001, 2012.
- 1346 [43] “Pileup Reweighting Procedure - <https://twiki.cern.ch/twiki/bin/viewauth/CMS/PileupReweighting>,”
1347
- 1348 [44] “Utilities for Accessing Pileup Information for Data - <https://twiki.cern.ch/twiki/bin/view/CMS/PileupJSONFileforData>,”
1349
- 1350 [45] “EGamma POG - Cut based electron ID for Run2 - <https://twiki.cern.ch/twiki/bin/view/CMS/CutBasedElectronIdentificationRun2>,”
1351
- 1352 [46] “EGamma POG - Electron ID recipes for Run2 - <https://twiki.cern.ch/twiki/bin/view/CMS/EgammaIDRecipesRun2>,”
1353
- 1354 [47] CMS Collaboration, “Performance of cms muon reconstruction in pp collision events at
1355 $\sqrt{s} = 7\text{TeV}$.” Submitted to *J. Inst.*, 2012.
- 1356 [48] R. Fruhwirth, “Application of kalman filtering to track and vertex fitting,” *Nuclear Instruments and Methods in Physics Research Section A: Accelerators, Spectrometers, Detectors and Associated Equipment*, vol. 262, no. 23, pp. 444 – 450, 1987.
- 1359 [49] “Reference muon id, isolation and trigger efficiencies for Run-II -
1360 <https://twiki.cern.ch/twiki/bin/view/CMS/MuonReferenceEffsRun2>,”
- 1361 [50] “Tau POG - Tau ID for Run2 - <https://twiki.cern.ch/twiki/bin/viewauth/CMS/-TauIDRecommendation13TeV>,”
1362
- 1363 [51] “EGamma POG - Cut based photon ID for Run2 - <https://twiki.cern.ch/twiki/bin/view/CMS/CutBasedPhotonIdentificationRun2>,”
1364
- 1365 [52] “JetMET POG - Jet ID for Run2 - <https://twiki.cern.ch/twiki/bin/view/CMS/JetID>,”
- 1366 [53] “Jetmet pog - jet energy resolution smearing - <https://twiki.cern.ch/twiki/bin/view/cms/jetresolution>,”
1367
- 1368 [54] A. J. Larkoski, S. Marzani, G. Soyez, and J. Thaler, “Soft Drop,” *JHEP*, vol. 05, p. 146,
1369 2014.
- 1370 [55] T. K. Arrestad et al., “Identification and calibration of boosted hadronic W/Z bosons at
1371 13 TeV,” tech. rep., AN-2016/215, 2016.
- 1372 [56] S. Chatrchyan *et al.*, “Identification of b-quark jets with the CMS experiment,” *JINST*,
1373 vol. 8, p. P04013, 2013.
- 1374 [57] “BTV POG - B-tagging for Run2 - <https://twiki.cern.ch/twiki/bin/view/CMS/BtagRecommendation80X>,”
1375
- 1376 [58] “Methods to apply b-tagging efficiency scale factors,” 2013.
- 1377 [59] CMS Collaboration, “Particle-flow event reconstruction in CMS and performance for jets,
1378 taus, and E_T^{miss} ,” no. CMS-PAS-PFT-09-001, 2009.